Fall 2011

On the Downstream Evolution of the Mean Momentum Field in Turbulent Shear Wake Flows

Marc R. Bamberger
University of New Hampshire, Durham

On the Downstream Evolution of the Mean Momentum Field in Turbulent Shear Wake Flows

BY

Marc R. Bamberger

B.S., University of New Hampshire (2009)

THESIS

Submitted to the University of New Hampshire
in partial fulfillment of
the requirements for the degree of

Master of Science

in

Mechanical Engineering

September 2011

ProQuest LLC
789 East Eisenhower Parkway
P.O. Box 1346
Ann Arbor, MI 48106-1346

Table of Contents

List of Tables

List of Figures

ABSTRACT

On the Downstream Evolution of the Mean Momentum Field in Turbulent Shear Wake Flows

by

Marc R. Bamberger
University of New Hampshire, September, 2011

The evolution of shear wake flow formed from the interaction of two turbulent boundary layers was investigated. Primary interest was given to the post-separation region, very close to the trailing edge of the splitter plate. Two velocity ratios and two trailing edge geometries were explored. Data were acquired using four-element hotwire traverses for multiple downstream locations. With these data sets, a comparison to DNS data, the mean streamwise velocity and its wall normal gradients, Reynolds stress and its gradient, velocity intensities, the mean momentum balance were analyzed. A primary finding is that, post-separation, the inertial terms in the mean momentum equation rapidly obtain leading order importance everywhere. Like in the boundary layers, the mean effect of turbulent inertia changes sign between wake center and the freestream. In this case, however, the change in sign denotes a change in the sign of the mean advection and Reynolds stress gradient term.

Chapter 1

Introdution

The present study investigates the transition of two wall bounded flows into a shear-wake flow, and subsequently into a mixing layer flow (see 1-1). Separate turbulent boundary layer flows having an absolute velocity ratio of 2:1 or 1:1 develop on opposite sides of a splitter plate. At the end of the splitter plate (i.e. the point of separation or trailing edge) the solid boundary ceases and the two flows interact. The development of the flow structure within this post-separation zone is of primary interest, as this region lies in between the boundary layer inflow and mixing layer outflow conditions. Important elements affecting flow development include the upstream differences in velocity of each flow, opposing signs of vorticity, and the momentum deficit between the two layers at the point of separation. With downstream distance, the momentum deficient shear wake region evolves into a free shear flow, which has a single sign of mean vorticity (see figure 1-1).

Due to the "no slip" condition, fluid velocity must match the wall velocity at the wall-normal height of zero. This creates a boundary layer with high momentum fluid in the free stream, and a decreasing distribution of mean momentum as the wall is approached. The turbulent boundary layers are created upstream of the separation point and have their primary mean gradient oriented in the wall normal direction from the splitter plate. The dynamics and structure of these boundary layers are very different from unbounded shear flows. In the canonical free shear turbulent flows (e.g. jets, wakes, mixing layers), the effects of viscosity on the mean flow rapidly become negligible, and the leading order of

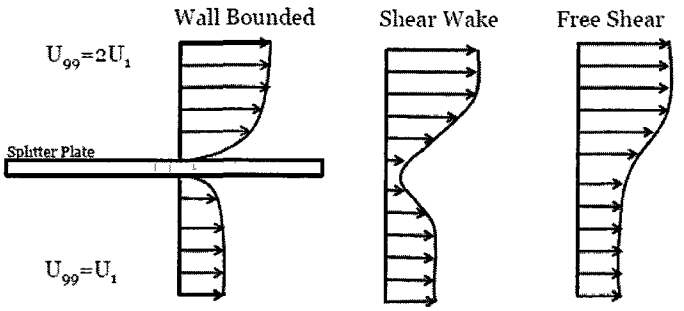

Figure 1-1: Mean streamwise velocity development

the mean dynamics are governed by inertial mechanisms [20]. However, in the presence of a wall, the mean viscous force is always of leading order in a region close to the boundary.

The differences in the wall bounded mean velocity profile to the free shear mean velocity profile are clearly illustrated in figure 1-1. The abrupt end of the splitter plate (separation point) creates a momentum deficient region between the two boundary layers, that constitutes the wake part of the shear wake flow component. In the absence of the boundary, the wall-region of the flow no longer absorbs momentum from the outer-region boundary layers. Instead, the inner regions of the two boundary layers, with opposing signs of vorticity, are able to interact and exchange momentum. These interations progress to create a smooth, mean streamwise velocity curvature in the low momentum region between the two boundary layers (see center profile of figure 1-1). The wake region eventually diminishes downstream as the two freestream flows add momentum to the inner region, and eventually the flow transitions to a two-stream mixing layer flow with a single sign of vorticity. Primary attributes of the evolution of this complex transition are discussed in following subsections.

1.0.1 Reynolds Shear Stress

Due to the large range of length scales (increasing with Reynolds number) within a turbulent flow, calculating or describing the flow in complete detail proves to be highly challenging. Owing to these complexities, one traditional approach, first proposed by Osborne Reynolds, involves decomposing the velocity field into a mean and fluctuating component, plugging this into the momentum equation, and averaging the result to produce the Reynolds-averaged Navier-Stokes equation [3]. Although not without its own challenges and ambiguities, this approach does allow one to focus on the mechanisms underlying the mean distribution of momentum and kinetic energy. Ensemble or time averaging the Navier-Stokes equations produces an average velocity field $\overline{u}(x,t)$. Further, we can use the Reynolds decomposition to separate the time average and fluctuating velocity components in the manner given by (1.1).

$$u(x,t) = \overline{u}(x,t) + u'(x,t) \tag{1.1}$$

Using the fact averaging is a linear operation (e.g. $\bar{u_i'} = 0$)[3], the Navier-Stokes equation for an incompressible, constant velocity flow can be simplified to:

$$\rho(\frac{\partial u_i}{\partial t} + \frac{\partial}{\partial x_j}\bar{u}_i\bar{u}_j) = -\frac{\partial \bar{p}}{\partial x_i} + \mu\nabla^2\bar{u}_i - \frac{\partial}{\partial x_j}R_{ij} \tag{1.2}$$

$$\frac{\partial u_i}{\partial x_i} = 0 \tag{1.3}$$

$$R_{ij} = -\rho\overline{u_i'u_j'} \tag{1.4}$$

The Reynolds decomposition, in concert with time averaging, has given rise to apparent stress-like quantities $-\rho\overline{u_i'u_j'}$, termed the Reynolds stresses, which couple the mean flow to the turbulence [6]. Under this description, the Reynolds stress tensor components essentially quantify the net mean flux of momentum caused by the turbulence.

The downstream evolution of the Reynolds stress profiles were investigated in this study in the same manner as the streamwise velocity. The evolution of the Reynolds

stress was found using time series data decomposed into mean and fluctuating components according to equaion (1.1). The Reynold stress profiles were normalized using the friction velocity (u_τ) measured from the boundary layer in the high velocity flow at the trailing edge. The wall bounded flow produces a Reynolds stress profile that starts at zero at the wall and rapidly rises to a peak near the wall [21]. The position of this peak varies with Reynolds number, and the peak value has a magnitude near unity.

Mixing in the shear-wake regime is intense, as the inner regions of the shear layers interact to create large turbulent fluctuations. Downstream of the separation edge, the absence of a boundary induces a rapid growth in the Reynolds stress peaks. Further downstream, these peaks decay until there is a single Reynolds stress peak in the mixing layer region that is offset slightly towards the high velocity side [16]. Figure 1-2 depicts the evolution of the Reynolds stress from boundary layer to mixing layer flow. An interesting observation is that the Reynolds stress initially increases dramatically in the shear wake region.

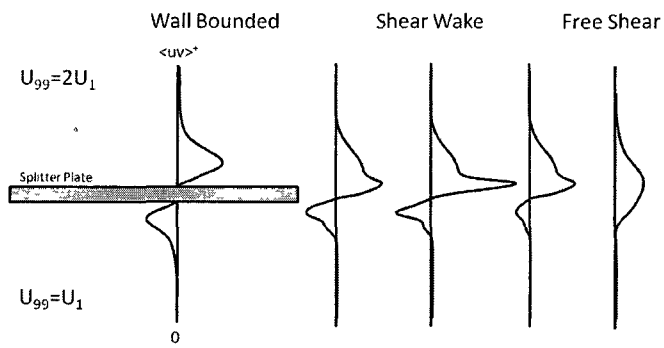

Figure 1-2: Mean Reynolds stress development

1.0.2 Mean Vorticity

Although vorticity is not a new concept in fluid dynamics, its time resolved measurement has proved not to be as simple as velocity and pressure measurement techniques. This is primarily because it requires accurately measuring velocity differences over very small distances. Vorticity is mathematically defined as the curl of velocity ($\vec{\omega} \equiv \nabla \times \vec{u}$). The expansion of this definition for a Cartesian coordinate system is given by equation (1.5).

$$\vec{\omega} = (\frac{\partial w}{\partial y} - \frac{\partial v}{\partial z})\hat{i} + (\frac{\partial u}{\partial z} - \frac{\partial w}{\partial x})\hat{j} + (\frac{\partial v}{\partial x} - \frac{\partial u}{\partial y})\hat{k} \tag{1.5}$$

Like velocity, vorticity can also be decomposed into mean and fluctuation parts. A two dimensional assumption for the mean flow simplifies this equation, and in the mean we are left only with vorticity in the z-direction.

$$\vec{\omega} = \bar{\omega}_z \approx -\frac{\partial \bar{u}}{\partial y}\hat{k} \tag{1.6}$$

The magnitude of the mean vorticity profile in the canonical wall-bounded turbulent flow is largest right at the wall, and with increasing distance from the wall smoothly approaches zero. It is important to note that mean vorticity profiles in the pre-separation boundary layers are of opposing sign. Also, the magnitude of vorticity at the wall is larger in the high speed flow than the low speed flow. These characteristics lead to some interesting phenomena when the boundary is removed and the two vorticity profiles merge. In the shear wake region, interactions between the strongly opposing sign inner layers of the vorticity profiles undergo annihilation, and thus the peak vorticity amplitude decreases. This cancelling of vorticity evolves downstream until the free shear region where the larger magnitude of vorticity in the high velocity flow eventually dominates. Figure 1-3 illustrates this progression from opposing sign to single sign vorticity.

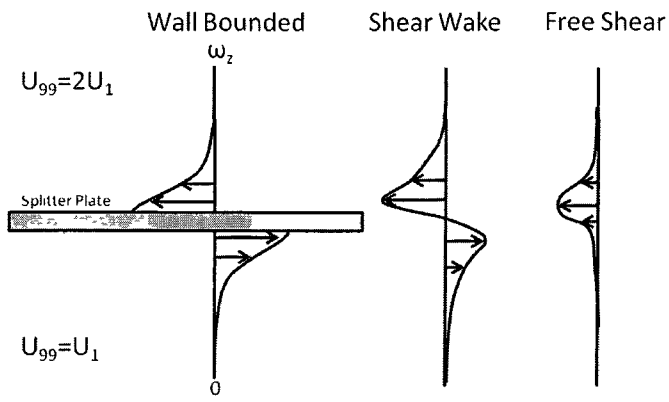

Figure 1-3: Mean streamwise vorticity development

1.0.3 Mean Momentum Balance

The development (or redistribution) of the momentum field in the transition from shear-wake to free shear flow can be studied by looking at the mean momentum balance directly. The mean momentum equation in a turbulent boundary layer contains three terms: mean advection (A), viscous stress gradient (B), and the Reynolds stress gradient (C). It is important to note that these are mean quantities, and therefore do not directly describe the instantaneous dynamics of the flow. However, it is true that the ensembles of the instantaneous flow combine to reflect the mean. The mean momentum balance terms are defined below in equation (1.7), where letters A, B, and C are used in subsequent figures.

$$\underbrace{U^+\frac{\partial U^+}{\partial x^+} + V^+\frac{\partial U^+}{\partial y^+}}_{A} = \underbrace{\frac{\partial^2 U^+}{\partial y^{2+}}}_{B} - \underbrace{\frac{\partial \overline{uv}^+}{\partial y^+}}_{C} \tag{1.7}$$

As initially shown by Wei et al in 2005, the ratio of the viscous stress gradient (B) to Reynolds stress gradient (C) reveals a distinct four layer structure in a turbulent boundary layer, shown in figure 1-4 [24]. The four regions found in the turbulent boundary layer are as follows:

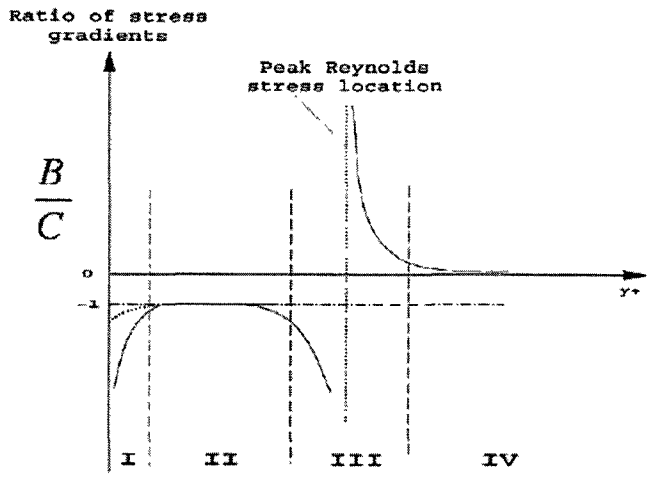

Figure 1-4: Depiction of the mean momentum balance for turbulent wall bounded flows adapted from Wei et al. [24]

- Region I: In the inner most layer the balance is between mean advection and the viscous stress gradient. The mean viscous force decreases with distance from the wall. In the zero pressure gradient case, all three terms of the mean momentum balance are zero at the wall, as is the net flux of vorticity [24].

- Region II: The viscous stress gradient and Reynolds stress gradient are essentially in balance. These terms are equal, but opposite, creating a constant ratio having a value approximately equal to negative one.

- Region III: In this layer, all three terms are of the same order of magnitude. The peak in the Reynolds stress causes the gradient to pass through zero, forming a discontinuity in the ratio of the terms (B) to (C) in layer three.

- Region IV: The viscous forces become negligible in the outer most layer, and the dominant order balance is between the mean advection and Reynolds stress gradient terms.

This four layer structure present in the pipe, channel, and turbulent boundary layer flows is investigated in full detail in Wei et al [24] and subsequent investigations [12]. In fully developed pressure driven flows, the term analogous to the mean advection in the boundary layer is the pressure gradient. The four layer structure, however, remains the same.

When the flow evolves into a free shear flow the layer structure is reconfigured. The Reynolds stress gradient becomes much larger than the viscous stress gradient for all wall normal positions (see figure 1-5). This is known from previous data, as well as shown by the current study. Considering the mean momentum balance in the mixing layer, we can assume that a 2-D shear wake should be the same for any "thin" shear flow, and thus satisfies the conditions associated with the boundary layer approximation. The mean momentum balance contains the same three terms as equation (1.7), but now the entire flow is, to leading order, dominated by inertia. The complexity of the evolution from the four layer structure of figure 1-4 to the single layer structure of Figure 1-5 is essentially undocumented, and thus is a primary focus of the present investigation.

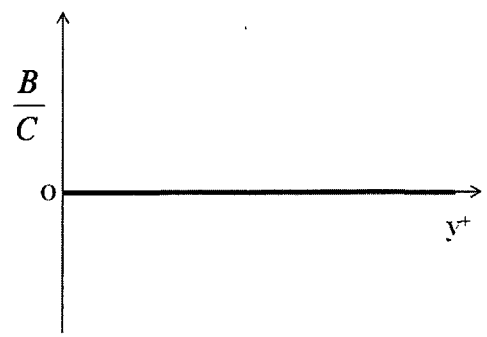

Figure 1-5: Mean momentum balance for free shear flows

The objective of this experiment is to better understand the complexities involved in the downstream evolution of a shear wake flow. An array of tools will be utilized in this

analysis. Mean velocities profiles will illustrate how the inward diffusion of momentum progresses from the shear wake, to the mixing layer flow. The varying mean magnitude of fluctuations in the fluid momentum will be examined by the Reynolds stress profiles. Lastly, the balancing of terms in the mean momentum equation will show whether stress gradients or mean advection are of leading order. Together, these tools will provide a context for describing the mean dynamics of shear-wake evolution.

1.1 Review of Previous Shear Layer Research

Past studies of the downstream evolution of a wall bounded to a free shear turbulent flow have been investigated relative to single and dual stream shear layers (Morris & Foss [17]), plane mixing layers (R.D. Mehta [16]), and coaxial jets (Dahm et al. [5]). These studies have examined the effects of differing velocity ratios, absolute velocities, and separation lip geometries. Better understanding the turbulence mechanics in shear layers play an important role in characteristics in aerodynamics, aeroacoustics, and the mixing of two streams.

1.1.1 Turbulent Boundary Layer to Shear-Wake Studies

The post-separation evolution of a turbulent boundary layer to a single stream shear layer was studied by Morris & Foss [17]. Separation of a primary turbulent boundary layer flow ($Re_\theta = 4650$) was caused by a sharp 90° edge. An entrainment flow perpendicular to the primary flow, with magnitude 28.5 times less than the primary free stream velocity, was used to regulate the single stream shear layer development. Using data acquired from hotwire anemometry, Morris and Foss concluded that only the near-wall vortices participate in the initial shear layer instability at the separation edge [17]. This "sub-shear layer" also allows for a physical explanation for why a shear layer will approach self-similarity at smaller x/θ values if, at separation, the flow is turbulent rather than

laminar. A schematic of the different flow regions in the post-separation section was also established from the data (see figure 1-6).

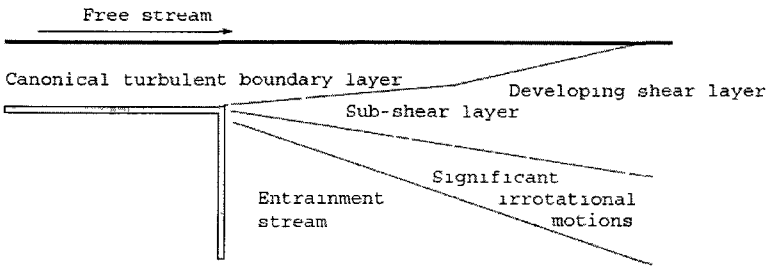

Figure 1-6: Flow regions in a single shear layer flow [17]

The interactions between inner and outer regions of a boundary layers were investigated by Hamelin & Alving [7]. The inner layer of a turbulent boundary layer was removed via a moving wall on the floor of the wind tunnel, which created a dramatic reduction in the mean wall shear and Reynolds stress levels. However, in the outer half of the boundary layer the Reynolds stress levels remained unchanged. Also, the ratios of Reynolds stresses in the outer layer are even less affected. From this, Hamelin & Alving concluded that "there is little sign of fundamental changes to the outer layer structure" when the inner layer is removed [7].

An important characteristic of the flow presently under investigation is that a two steam shear layer contains both signs of vorticity (Ω_z). In the both studies from Morris & Foss and Hamelin & Alving, only a single sign of vorticity was present in the flow. Likewise, both concluded that the post-separation, outer boundary layer region remained statistically the same for a considerable distance downstream. The current study will observe if this insensitivity of the outer to the inner region remains plausible with different upstream conditions.

1.1.2 Effect of Velocity Ratio on Mixing Layer

R.D. Mehta completed a study that investigated the effect of velocity ratio on plane mixing layer approaching self-similarity [16]. The facility employed was a near identical mixing layer tunnel used in the current study. In Mehta's study, the two legs of the tunnel were powered by different capacity blowers (5,000cfm and 15,000cfm). This allowed for a wide range of velocity ratios to be attained (0.5, 0.6, 0.7, 0.8, and 0.9), whereas in the current study a velocity ratio of 0.5 is utilized. A cross-wire, tungsten element probe measured mean flow and turbulence data at eight streamwise locations. The upstream boundary layers were tripped into turbulence as in the current study.

The results from Mehta's study indicated that the splitter plate wake plays a very dominant role in the downstream development of the mixing layer [16]. In the higher velocity ratio cases (0.8 and 0.9), the mixing layer did not reach self similarity within the measured downstream distance. However,it was apparent that further downstream self-similarity would inherently be achieved. At lower velocity ratios (0.5 to 0.7), self-similarity of the mixing layer was observed. These velocity ratios satisfied all three necessary conditions: linear growth, asymptoting of the peak Reynolds stresses to constant values, and collapse of the mean flow and turbulence profiles in similarity coordinates [16]. Mehta concluded that the downstream distance in which self-similarity is achieved decreases with increased velocity ratio from 0.5 to 0.7. As velocity ratio increases higher than 0.7 this relationship is reversed, such that an increase in velocity ratio increases the distance to similarity.

1.1.3 Coaxial Jets

The near field of a coaxial jet has been under investigation for more than twenty years, largely to provide a solution to reducing the flow noise associated with simple jets. In the past, it has been empirically proven that the combined noise of a coaxial jet surrounding an inner jet can be lower than the inner jet by itself. Providing a quieter means of jet

propulsion can be advantageous to military and civilian jet powered vehicles.

Dahm et al. examined coaxial jets using laser induced fluorescence to visualize different flow variations (velocity ratio and absolute velocities) [5]. Certain flow phenomena, such as "locking", were clearly observed in the LIF photographs. Dahm defined locking as two vortex layers that are not developing independently of each other, making the two vortex frequencies about the same. Evidence of this locking is seen in the error between the experimental vortex passage frequency ratio to the calculated value "F" assuming the two concentric layers develop independently (1.8).

$$F = \left(\frac{U_1 + U_2}{U_2 + U_3}\right)^2 \frac{|U_2 - U_3|}{|U_1 - U_2|} \tag{1.8}$$

Where U_1, U_2, and U_3 are the absolute velocities of the inner jet, outer jet, and surrounding fluid, respectively. In a few cases, the calculated and experimental frequency ratio differed by more than a factor of ten.

This experiment also disproved the conclusions made in 1976 and 1977 by Kwan and Ko [13, 14] by indicating that coaxial jets cannot simply be treated as a "combination of several single jets". Instead, coaxial jets are found to be much more complicated, and dependent on each individual jet's properties. Three LIF images from the study of Dahm are shown in figure 1-7, these illustrate the effect of velocity ratio on the vortex structure which can be seen in all three, but differ in number, size, and frequency.

1.1.4 Previous Masters Theses

The two stream shear layer facility used in this study was employed in previous Master's Thesis studies. These were completed by Challa [2] and Wait [23]. Initially, Wait investigated the laminar initial condition shear-wake flow by using single element hotwire anemometry to acquire streamwise velocity statistics (mean, RMS, skewness, kurtosis, and streamwise velocity spectra). Three different trailing edges (blunt, round, and sharp) were utilized at three different velocity ratios (1.00, 0.75, 0.5). Wait concluded that the

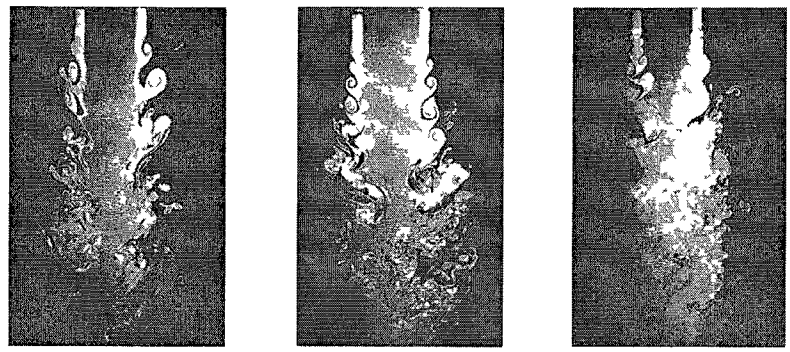

(a) $U_1/U_2 = 0\ 59$ (b) $U_1/U_2 = 1\ 14$ (c) $U_1/U_2 = 2\ 56$

Figure 1-7: Coaxial Jets with varying velocity ratios ($U_1 = .11m/s$ and $U_3 = 0m/s$ in all cases) [5]

round and blunt trailing edges had similar flow properties, while the sharp trailing edge differed A velocity ratio of 1 0 formed a symmetric profile about y=0. A VR=0.75 induced a shift in the mean profile troughs toward the low velocity side while increasing the shear-wake width. A VR=0.5 (the case present in this study as well) stimulated a much faster evolution from shear-wake to mixing layer.

Subsequently, Challa repeated the study done by Wait but with turbulent boundary layers at the separation lip. She used a single velocity ratio of 0.5, as in the present study. The boundary layer upstream of the separation lip was tripped to turbulence by a strip of sandpaper. Again, it was concluded that the round and blunt trailing edges exhibited similar flow properties, and the sharp trailing edge differed The transition from turbulent boundary layer to shear-wake flow with the round and blunt edge occurred in half the downstream distance as the sharp edge. The shear-wake width was also found to be nearly independent of downstream position.

1.2 Scope of the Present Experiment

The present experiments investigate the downstream evolution of two wall bounded, turbulent boundary layers into a shear wake flow, and finally into a free shear flow. The experiment was performed in a dual shear layer tunnel where two separate turbulent flows meet at a blunt or sharp trailing edge. Three cases were investigated: sharp edge without shear (velocity ratio of 1:1), sharp edge with shear (velocity ratio of 2:1), and blunt edge with shear (velocity ratio of 2:1). Profile data were acquired using a four-element, hotwire probe in a "vorticity" configuration. Data were acquired at up to eight downstream locations between 1.76θ ($\approx 3.8mm$) and 158.75θ ($\approx 342.9mm$). In all cases, θ is the momentum deficit thickness of the high-speed flow at the trailing edge. From these measurements the evolution of the mean velocity and its wall normal gradient, Reynolds stress and its gradient, and the mean momentum balance. In addition, the shear wake data closest to the point of separation were compared to turbulent boundary layer data at roughly the same δ^+ values. This turbulent boundary layer data comes from a direct numerical simulation performed by Schlatter et al. [19]. In this comparison mean streamwise velocity and its wall normal gradient, and velocity intensities were examined. Investigation of these areas will give a better understanding of the mechanisms involved in the transition from one type of turbulent flow to another.

1.3 Motivation

In previous studies, the mean momentum balance been analyzed in boundary layers formed under various flow conditions. A recent study by Klewicki et al. [11], investigated the mean momentum balance in transitional boundary layers. The mean momentum balance of a rough-wall turbulent boundary layer is under investigation by Mehdi et al. [15]. The motivation for this study was to explain the mean dynamics as the four-layer

structure of the turbulent boundary layer observed in previous studies evolves into the mixing layer balance that is solely comprised of inertial terms. This required performing a physical experiment in a two stream shear layer tunnel, and capturing the necessary data to analyze the terms in the mean momentum equation for increasing downstream distance. These results can be related to physical applications, such as coaxial jets, to better understand the mechanics of shear layers in general.

Chapter 2

Experiment

2.1 The Facility

The experiments were performed in a large-scale two-stream shear layer tunnel located in Kingsbury Hall at the University of New Hampshire. A schematic of the facility is shown in figure 2-1. This tunnel is comprised of two centrifugal blower fans powered by two frequency driven motors. The frequency drives were controlled separately by two decade resistors mounted on the outside of the tunnel. This two-blower configuration allows for a shear flow to be formed when the separate streams are operated at different velocities. The centrifugal blowers have permanently fixed-pitch blades so the tunnel velocities are approximately restricted to between 2 m/s and 20 m/s. At velocities lower than 2 m/s, there is a large amount of buffeting in the flow caused by the large blower blades slowly rotating. The air velocities on each side of the splitter plate were monitored via two Pitot static tubes mounted through the top of the tunnel at the beggining of the splitter plate.

Downstream of the centrifugal blowers, each flow stream accelerates through a contraction with a ratio of about 3:1, and a turbulence management section. The turbulence management section consists of a honeycomb screen and seven smaller screens that reduce the streamwise turbulence intensity. The turbulence intensity values are discussed in the following section. After the contraction, the flow enters the approximately four meter long test section. A 7.6 centimeter wide strip of 50 grit sand paper is used to trip the boundary layer to turbulence about 1.2 meters upstream of the separation lip (end of plate).

These turbulent boundary layers grow along the 119 centimeter long splitter plate. The shear flow is two-dimensional, with flow properties being constant in the vertical direction (parallel to splitter plate but perpendicular to the main flow).

The outer walls of the tunnel are hinged at the start of the test section. This allows for the adjustment of the axial pressure gradient. In the present experiments these were set to maintain a zero pressure gradient as the boundary layer and shear-wake flows continue to grow in the x direction. The required wall divergence angle was found experimentally through use of two pitot-static tubes to measure the mean freestream velocity of the two streams. The pitot-static tubes were traversed upstream and downstream 0.5 meters from the separation lip in order to ensure full coverage of the test section. The wall divergence angles were controlled using two power screws located at the exit of the tunnel. A wall divergence angle of approximately 0.53° was found using *measure* and *adjust* iterations. Figure 2-1 gives a schematic of the test section dimensions and components within.

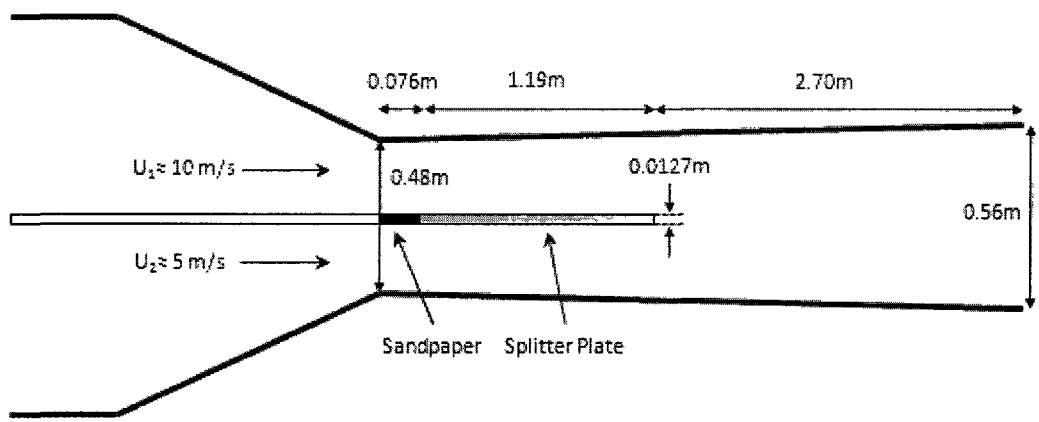

Figure 2-1: Schematic of the experimental facility test section

2.1.1 Trailing Edge Geometries

Two different splitter plate trailing edge geometries were utilized in this study: blunt and sharp. The dimensions for each edge type are shown in figure 2-2. The edge type was mounted flush against the splitter plate, in order to insure a smooth flow transition from one plate to the other. Any cracks that were found between the two plates were sealed with insulation putty and trimmed level with a razor blade.

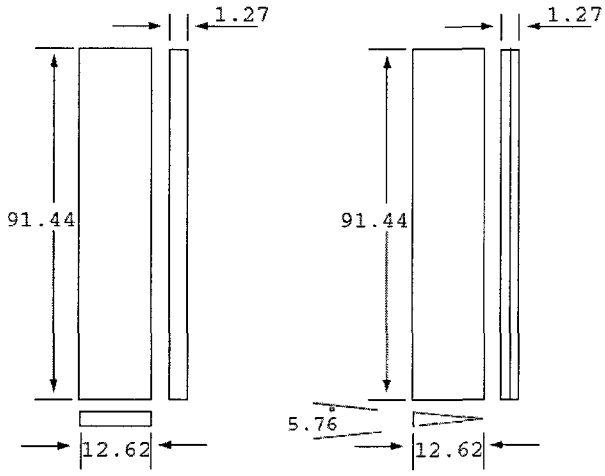

Figure 2-2: Dimensions of Blunt Edge (left) and Sharp Edge (right) (all in centimeters)

2.2 Equipment and Set-Up

A wide range of test equipment was used. These enabled the experimental procedure to be almost entirely automated, and reduced the amount of manual post-processing work. Computations were done with a LabVIEW PXI-1042, which was operated by Windows XP. The PXI computer was upgraded from 512MB to 4GB RAM for faster and extended capabilities. LabVIEW was used for programming and controlling all aspects of the

calibration and experimental procedures. The PXI computer has available slots for other modules such as data acquisition and motion control which made it more effective than a standard PC interface.

The PXI-6143 analog to digital converter used to acquire data has a 16-bit resolution and a maximum of 250k samples per second per channel. Up to eight analog inputs could be sampled simultaneously. The present experiments used four analog channels for a total load of 48kS/s.

An NI MID-7604 motion controller module was used to drive the four stepper motors used in the experiment. Two stepper motors (each rated for 3 volts, 4 amps) were connected to the Velmex traverses used to move the hotwire probe within the wind tunnel. The other two motors were used in controlling the pitch and yaw of the calibration nozzle needed for calibrating multi-wire hotwire probes. The yaw arm was driven by a 3.6 volt, 31.2 oz/in motor connected to a gear box with a 216:1 ratio. The pitch arm required more torque to hold the 64 oz flow nozzle on its 8 inch arm at all angles during a calibration process. A 5.5 volt, 100 oz/in motor connected to a chain and sprocket drive with a gear reduction of 70:1 was used. Figure 2-7 shows an image of the calibration set-up.

All pressure data for the two pitot tubes and calibration nozzle were acquired using MKS 698A Baratron high accuracy manometers. These transducers are internally heated for temperature stability, and have a full scale pressure range of 10 Torr, with $\pm 0.15\%$ accuracy. Manometer readings were regulated and controlled using an MKS 670 signal conditioner. The signal conditioner was connected via BNC cable to the PXI system for data acquisition.

The hotwire circuitry required to perform constant temperature anemometry was contained within the AN-1003 module made by AA Lab Sytems. This anemometer has up to 12 individual channels for 12 different hotwires that can all be run simultaneously. Each module contains nulling and damping potentiometers, 0-99.9 Ohm bridge balancing

decade resister, and signal conditioning options. Also, the AN-1003 has an adjustable 0-10 volt, 2 microsecond pulse for performing the square wave test for estimating and adjusting the hotwire response time. Each anemometer channel was connected via BNC to the PXI data acquisition board.

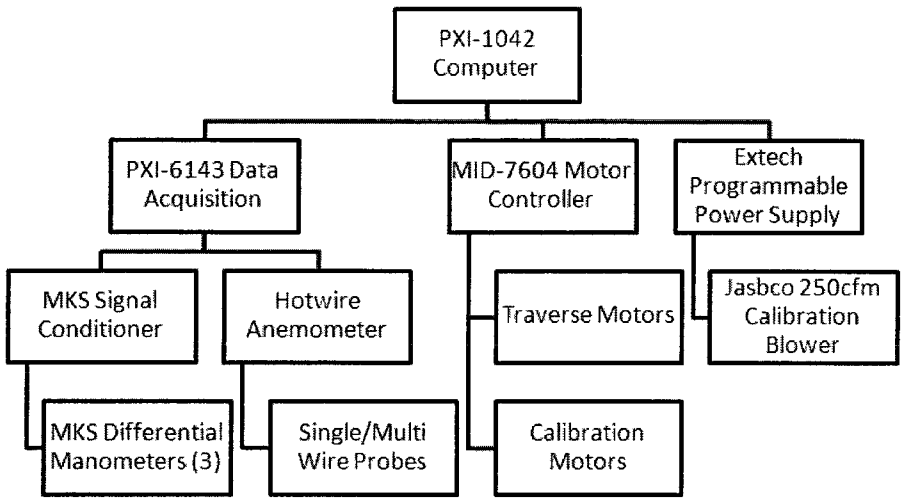

Figure 2-3: Equipment Hierarchy Chart

2.2.1 Hotwire Anemometry

Hotwire anemometry has long been used for investigating laminar and turbulent fluid flows. A hotwire is comprised of a thin metallic element welded to larger prongs which is heated via electric current (known as the Joule effect). Lower temperature fluid flow over the surface of the wire convects heat away from the wire at a velocity dependent rate. The material properties of the wire govern how electrical resistance varies with temperature. This allows for a relation between fluid velocity perturbations and voltage to be found.

Hotwires have many positive attributes which often make them a more attractive choice in comparison to Laser Doppler Velocimetry (LDV) or Particle Image Velocimetry

(PIV). The high frequency response of hotwires (tens to hundreds of kHz range) have been utilized for accurately measuring the turbulent velocity fluctuations under numerous conditions [9]. For a properly designed experiment, the wire width is small enough that the measurements can be reasonably called "local" in space. Hotwires also have the ability to operate over a wide range of velocities. from subsonic to supersonic flows. The working fluid can also range in characteristics such as viscosity, phase, and physical make-up [9, 34-1]. Using a film in place of the thin wire enables higher viscosity fluids such as water to be analyzed with the same methods as air. As with most probes, a main disadvantage is the intrusiveness of physically putting the hotwire in the flow. Also, hotwires cannot distinguish the difference between reversing flows due to the symmetry of heat transfer on either side of a wire.

There are various techniques used in hotwire anemometry. Each method aims to hold a different variable constant (temperature or current) while allowing the other variables to fluctuate. In constant current anemometry (CCA), a constant source of current is supplied to the hotwire probe. The varying wire resistance gives a varying voltage measurement as heat is transferred from the wire to the working fluid. Constant temperature anemometry (CTA) requires an auxiliary feedback circuit (Wheatstone bridge) that supplies variable current to the wire in order to keep the resistance (and consequently the temperature) constant. The variation in current is then measured on a different leg of the bridge to provide a correlation to fluid velocity [9, 34-2]. The CTA method is used in the present experiments.

2.2.2 Probe Properties

A four element vorticity probe was employed for all experiments. This probe was designed and constructed in its entirety at the University of New Hampshire. The hotwire probe was designed to take advantage of smaller diameter sensing wires (relative to our existing

Figure 2-4: Four Element Vorticity Probe

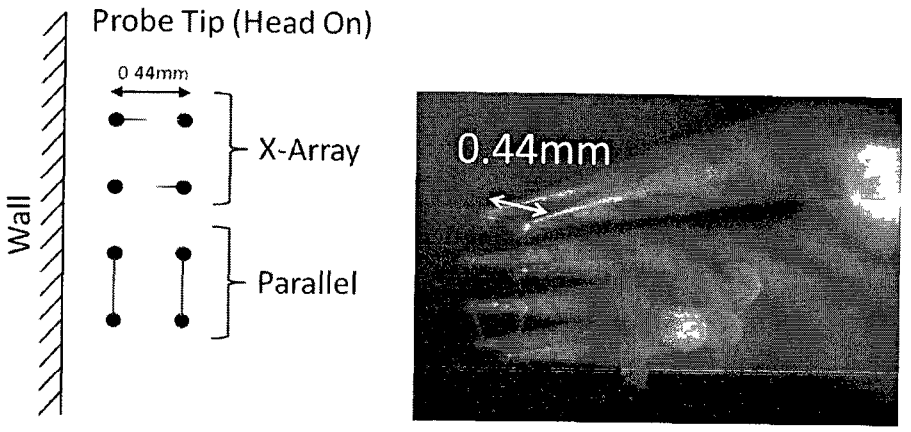

(a) Diagram of Probe Tip (b) Microscope Image of Vorticity Probe Tip

Figure 2-5: Vorticity Hotwire Probe Tip

sensors) for improved spatial resolution (see figure 2-4). The sensor wires had a diameter of $2.5\mu m$ and are made of Wollaston platinum with a 10% rhodium core. The prongs that support the sensor wire were constructed out of 304V stainless steel. The tip was tapered over a distance of 0.01 m with a final tip diameter of about $35\mu m$. Figure 2-5(a) and 2-5(b) shows the eight prongs that are arranged in an x-array and an adjacent parallel array. The two parallel wires have a length of 0.44 mm. The x-array wires are oriented at 45 degrees which increases the wire length to 0.62mm. The platinum wire has a resistance of $\approx 30\Omega$ per millimeter, causing the cold resistance of the x-array wires to be 5.5Ω greater than the parallel array wires. The A-A lab systems anemometer used can accommodate this increase in cold resistance, so it does not have an adverse effect on the frequency response of the x array wires.

2.3 Calibration

2.3.1 Calibration Apparatus

The hotwire calibration apparatus consists of a nozzle with flow straightening components mounted on a frame that can rotate in the pitch and yaw directions, and a blower box. The nozzle creates a top-hat jet profile with a large potential core that can vary from 2 m/s to 12 m/s. This jet is powered by a Jasbco 24 volt, 250 cfm flangemount blower attached to a one cubic foot box. The box acts as a pressurized plenum to reduce fluctuations caused by variations in motor speed. The pressurized box is connected to the nozzle by 1.25 inch diameter flexible hosing.

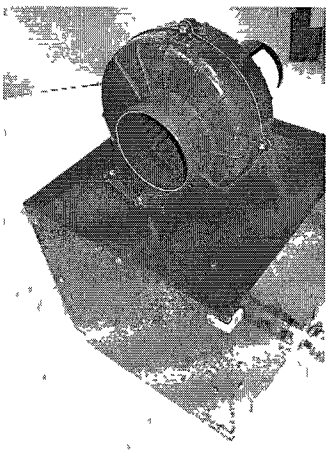

Figure 2-6: $1ft^3$ Box with 24V Blower

The flow velocity through the nozzle is controlled by regulating the voltage from an Extech programmable power supply. Pitot tube measurements at the exit of the nozzle were correlated to a pressure tap upstream of the nozzle. This allows for accurate nozzle exit velocity readings without having a Pitot tube disrupt or alter the core flow during the

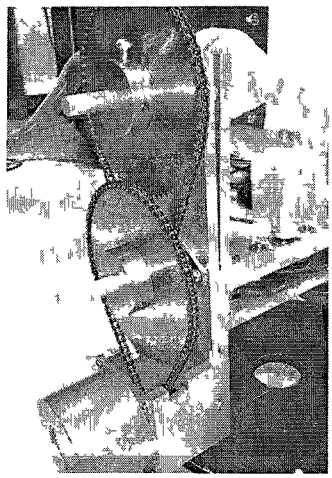

Figure 2-7: Dual axis laminar jet nozzle stand

actual hotwire calibration process Figure 2-8 shows the linear fit between the pressure before the nozzle and the stagnation pressure.

Since the nozzle does not remain stationary during calibration, the pressure drop in the flexible hose connecting the nozzle and plenum can vary. As the nozzle is rotated to extreme angles, the jet velocity changes slightly for a fixed blower setting In order to keep the exit velocity constant for each angle sweep, a proportional integral derivative (PID) controller was used. After the nozzle makes an angle change the velocity is checked again via the pressure tap measurement. If the nozzle velocity is outside of the user specified velocity tolerance, the controller adjusts the power supply voltage accordingly. A tolerance of 0.2m/s was used in order to keep the overall calibration time reasonable.

2.3.2 Single Wire/Parallel Sensors

The sensors oriented normal to the flow (single or parallel) were positioned such that the axis of the sensing element was parallel with the splitter plate and perpendicular to the mean velocity of the separating boundary layer. This allows for accurate measurement of

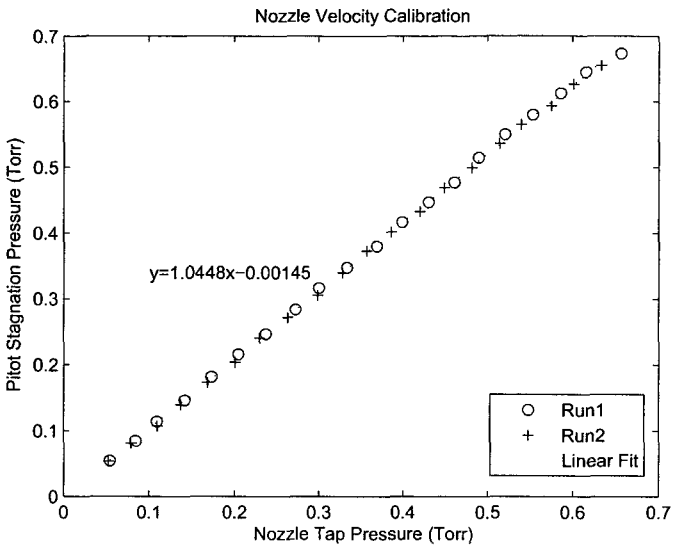

Figure 2-8: Nozzle pressure tap to dynamic exit pressure correlation

the boundary layer properties as the probe is traversed away from the wall. Calibrating normally oriented sensors only requires a laminar jet of variable velocity. The probe is calibrated before experiments and after to check for any drift. Drift is caused by the cyclic heating and cooling of the wire when it is in its operate mode. This effect diminished with increasing use of probe. Heating and cooling the wire can change the material properties of the wire which also changes the resistance. If minimal drift occurs, the average of the before and after calibration may be used in order to get better results (see Figure 2-9). For the sensors used herein, it was found that a third order polynomial (2.1) fit the calibration much better than King's Law ($E^2 = a + bU^n$), where the coefficients b and c are determined using a least squares linear regression. The polynomial coefficients were determined for using the *polyfit* function in Matlab.

$$U = a + bE + cE^2 + dE^3, \tag{2.1}$$

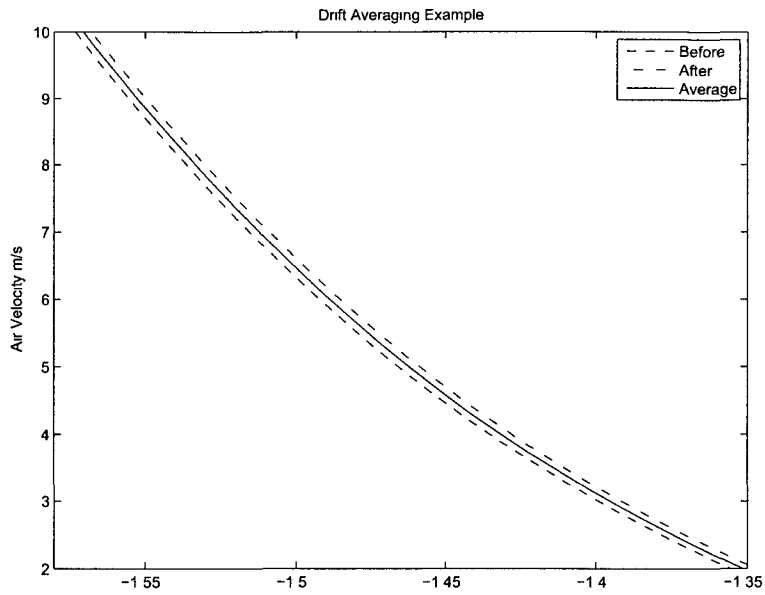

Figure 2-9: Single wire calibration using third order polynomial

2.3.3 Cross-Wire (x-array) Sensors

The two wire, x-array hotwire probe is designed to measure two velocity components; one in the direction of the mean flow, and the other perpendicular to the wall. The calibration of this probe requires an angle sweep around one axis at multiple velocities. In this case the nozzle stand is swung from +30° to -30° in 5° increments. Each sweep is done at a fixed jet velocity. within some predefined tolerance as described previously. Varying the jet angle across the x- array causes one wire to become more normal to the flow, while the other wire becomes more parallel to the flow. For wires that are inclined to the mean flow, an accurate expression for effective cooling velocity in a three-dimensional flow field is proposed by Jorgensen is given in equation (2.2) [10].

$$U_e^2 = U_n^2 + k^2 U_t^2 + h^2 U_b^2 \tag{2.2}$$

Where velocities U_n, U_t, U_b are the normal, tangential, and bi-normal component, respectively. The constants k and h correspond to error corrections due to tangential cylindrical

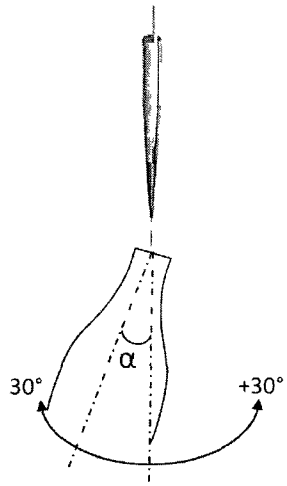

Figure 2-10: Articulating calibration jet showing jet angle α

cooling and prong blockage, respectively. The streamwise (u) and wall normal (v) velocities of the jet are calculated using,

$$u = U_{jet}cos(\alpha) \tag{2.3}$$

$$v = U_{jet}sin(\alpha), \tag{2.4}$$

where U_∞ is the nozzle jet velocity and α is the nozzle angle (see figure 2-10). Further details on cross-wire calibration methods can be found in Vukoslavevic et al. [22]. In figure 2-11 both the measured and calculated u and v velocities are shown. On the left, each inverted "U-shaped" curve signifies one -30° to 30° sweep, where the jet velocity increases after each sweep. On the right, it can be seen that the v velocity is symmetric about $\alpha = 0°$, where the velocity is intuitively also zero. Also, note the close correspondence between the measured and calculated data points for both plots, signifying a high fidelity calibration.

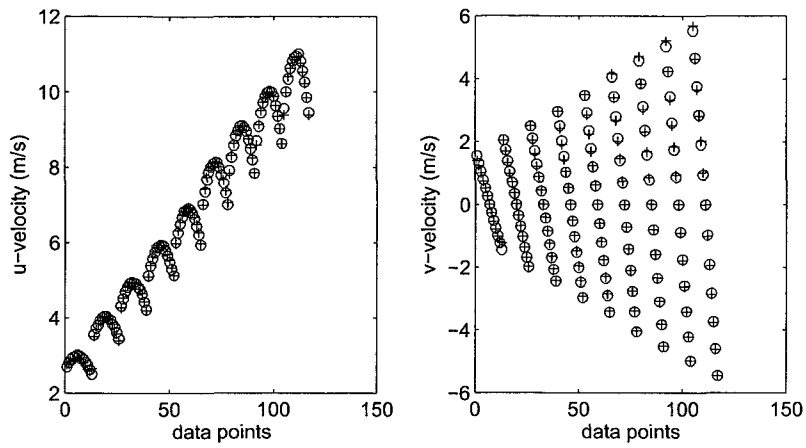

Figure 2-11: Calibration example of an X array hotwire (Measured:O, Calculated:+)

2.4 Measurements and Statistics

Single and multi-wire probes were used to measure streamwise and wall normal velocity components. The use of Reynolds decomposition segregates the instantaneous velocity into mean and fluctuating components (e.g., $\tilde{u} = U + u$). The free stream velocities are denoted as $U_{\infty,10}$ and $U_{\infty,5}$ for the 10 m/s and 5 m/s sides of the splitter plate. This section presents the equations and describes the ana lyses used to characterize the turbulent flows under investigation.

2.4.1 Turbulence Intensity

The turbulence intensity characterizes the streamwise turbulence with respect to the free stream velocity. More specifically, turbulence intensity is the standard deviation of the velocity fluctuations over the mean free stream velocity.

$$I \equiv \frac{u'}{U_\infty} \tag{2.5}$$

In the free stream velocities of 10 m/s and 5 m/s, the average turbulence intensity was 0.32% and 1.58%, respectively. In an effort to lower the turbulence intensity of the

5 m/s leg of the tunnel, worn seals between the blowers and tunnel contractions were replaced. Unfortunately, this did not have an effect on the turbulence intensity. The evidence provided later indicates that the increased intensity in the slower velocity stream is probably attributable to blade-passing unsteadiness from the blower running so close to the minimum speed. While this freestream intensity is quite large, the analysis herein provide little reason to believe that the conclusions derived are substantively influenced.

2.4.2 Statistical Profiles

In order to better understand and visualize the progression from wall bounded flow to free shear flow, a four-wire, vorticity probe was used to acquire the mean and RMS profiles of the streamwise and wall normal velocities. Most of the profile data were normalized in the wall normal (y) direction by using the shear wake width (δ_{sw}) to obtain the scaled cross-stream coordinate (η) at each position. The streamwise distances downstream were normalized by the momentum thickness (θ). Both of these normalizing parameters are descibed later in section 2.4.5.

The mean velocity was calculated at each transverse location using equation (2.6).

$$U = \frac{1}{n}\sum_{i=1}^{n}\tilde{u} \tag{2.6}$$

The RMS velocity was also calculated at each transverse location using equation (2.7).

$$u_{RMS} = \sqrt{\frac{1}{n}\sum_{i=1}^{n}(\tilde{u} - U)^2} \tag{2.7}$$

In these equations, n is the total sample size, and $\tilde{u} = u + U$.

2.4.3 Integral Properties

The thickness of the boundary layer can be characterized by δ_{99}, which is the distance from the surface (or maximum wake deficit) to where the mean velocity is 99% of the

free stream velocity [8]. Two more precisely defined integral properties are the mass and momentum deficit thicknesses. The mass deficit thickness (or displacement thickness), denoted by δ^* in (2.8), is the distance the plate would be moved so that the loss of mass flux (due to reduction in uniform flow area) is equivalent to the loss the boundary layer causes [8]. The momentum deficit thickness is denoted by θ in (2.9), and for the flat plate flow, is equal to the lost free stream momentum flux in the boundary layer attributable to the shear force at the wall.

$$\delta^* = \int_0^{\delta_{99}} (1 - \frac{U}{U_\infty}) dy \tag{2.8}$$

$$\theta = \int_0^{\delta_{99}} \frac{U}{U_\infty} (1 - \frac{U}{U_\infty}) dy \tag{2.9}$$

2.4.4 Spectral Intensity Distributions

While a general spectral analysis is beyond the scope of the present study, spectra were used in the experimental design. The distributions of spectral intensity (power spectra) were determined using Welch's method with a window size of 2^{12} samples and an overlap of 2^{11} samples. An important initial use of spectra was to determine the sampling frequency rate for the hot wire experiments. By examining the distribution of power associated with the frequencies within the velocity time series at each wall normal position, a maximum turbulence frequency can be estimated (see figure 2-12). The flow was originally profiled at a rate of 15 kHz for 60 seconds. From the spectral intensity plots it was determined that the maximum frequency in high and low velocity free streams were 250 Hz and 800 Hz, respectively. The higher frequencies can be attributed to the slow fan speed required for the low velocity flow. The highest frequencies of about 5000 Hz were seen right behind the plate. From these analyses, the sampling frequency was lowered to 12 kHz which is more than twice that of the highest frequency seen, satisfying the Nyquist frequency. The sampling time was lowered to 40 seconds, which allows for an eddy the diameter of the

Table 2.1: Turbulence Frequency Range at $\delta_{sw} = -\frac{1}{2}, 0, \frac{1}{2}$

δ_{sw} *Location*	Max Frequency Recorded (Hz)
$\delta_{sw} = +\frac{1}{2}$ ($\approx 10\frac{m}{s}$)	250
$\delta_{sw} = 0$	5000
$\delta_{sw} = -\frac{1}{2}$ ($\approx 5\frac{m}{s}$)	850
Sampling Freq Used	12000

largest boundary layer thickness ($\delta_{99} \simeq 20mm$), in the lowest speed flow (5 m/s), to pass by the sensor about 10,000 times.

2.4.5 Non-Dimensional Variables

Friction Velocity

The friction velocity, denoted as u_τ, was used to normalize streamwise and wall normal velocities in the early, boundary layer part, of the shear-wake flow development. The friction velocity is the characteristic velocity for turbulent wall-flows [18]. It is defined as $u_\tau = \sqrt{\tau_w/\rho}$. Obtaining an accurate measurement of the mean wall shear stress (τ_w) can prove to be difficult, involving additional devices such as floating-element sensors [21, 880]. A common indirect method for estimating the wall shear stress involves use of the Clauser plot. For the canonical flat plate flow, this method estimates u_τ within reasonable accuracy (about $\pm 5\%$) [21]. Clauser observed that the wall shear stress in a turbulent boundary layer could be estimated relatively accurately through the correlation with the logarithmic law of the wall (2.10). In this method, the slope of the logarithmic portion of the time averaged velocity plot is matched with the corresponding skin friction coefficient ($C_f = 2(u_\tau/U_\infty)^2$) to estimate for the wall shear stress (see figure 2-13). This

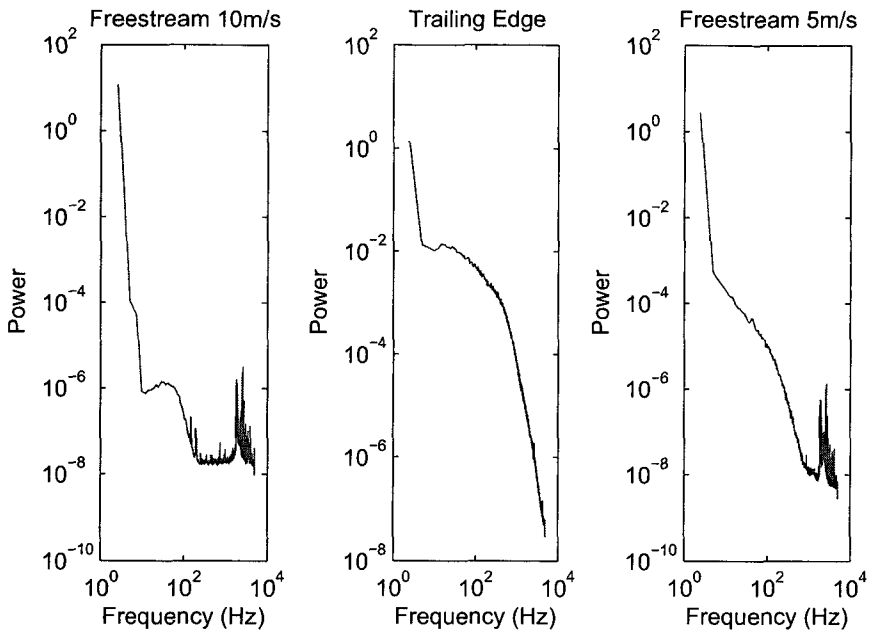

Figure 2-12: Spectral intensity plots at $x = \theta$ and three wall normal positions

is an attractive method since difficult to acquire velocity measurements in the viscous sublayer are not required. For further information on this technique see Clauser [4].

The slope of the "log law" region is defined by equation (2.10), and the friction velocity is then estimated using the definition of y^+ (equation (2.11)).

$$U^+ = \frac{1}{k} ln(y^+) + C \tag{2.10}$$

$$y^+ = \frac{y u_\tau}{\nu} \tag{2.11}$$

Where C and k are constants. For the present experiments C=5.0 and k=0.41 were used [21]. Table 2.2 lists all the friction velocity values estimated for both freestreams at all downstream distances. In the result section, however, the friction velocity estimated from the high speed flow closest to the separation lip was used to normalize all parameters ($u_\tau = 0.457 m/s$).

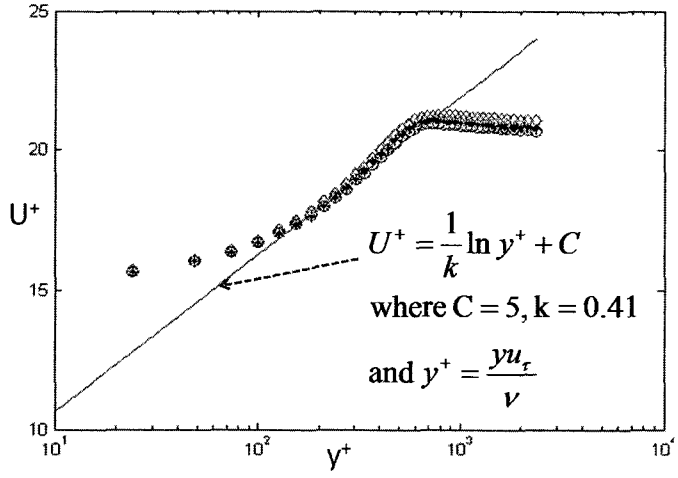

Figure 2-13: Inner Normalized Mean Velocity (U^+) showing "law of the wall"

Table 2.2: Friction velocity values at increasing x/θ in high and low velocity flows

Streamwise Distance	u_τ	
(x/θ)	5 m/s	10 m/s
1.76	0.229 $\frac{m}{s}$	0.433 $\frac{m}{s}$
2.94	0.258 $\frac{m}{s}$	0.427$\frac{m}{s}$
11.76	0.250 $\frac{m}{s}$	0.419 $\frac{m}{s}$
41.16	0.237 $\frac{m}{s}$	0.394 $\frac{m}{s}$
158.75	0.235 $\frac{m}{s}$	0.375 $\frac{m}{s}$

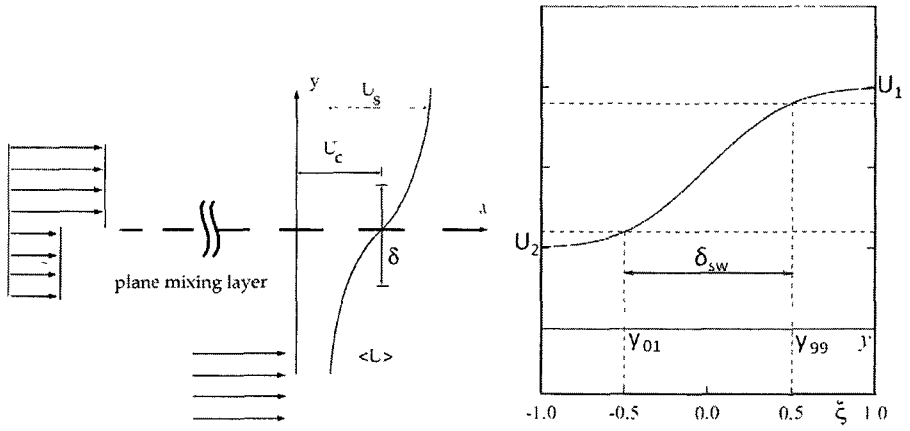

(a) Mixing Layer Diagram

(b) Mean Velocity U with definitions (where, $\xi = \eta$)

Figure 2-14: Defining the scaled cross-stream coordinate parameters [18]

Scaled Cross-Stream Coordinate

As the separated boundary layers develop downstream, the flow increasingly develops its free shear flow characteristics. Owing to this, free shear characteristic lengths become increasingly relevant (as opposed to boundary layer parameters). One of the lengths employed to normalize the wall normal distance (y) is the scaled cross-stream coordinate η [18]. This length is based on the characteristic width of the shear flow $\delta_{sw}(x)$, defined as:

$$\delta_{sw} = y_{0.99}(x) - y_{0.01}(x) \tag{2.12}$$

Where $y_{0.99}$ and $y_{0.01}$ are distances to 99% of the respective free stream velocities. The scaled cross-stream coordinate η is defined as:

$$\eta = y/\delta_{sw}(x) \tag{2.13}$$

A sketch of mean streamwise velocity versus the scaled cross-stream coordinate is included in figure 2-14.

2.5 Experimental Procedure

Initially, the probes were mounted in the universal probe stand, such that that the center of the probe tip was in the center of the calibration nozzle at the exit plane. The square wave test was performed on all senor wires in order to optimize the dynamic response of the instrument. The square wave was generated using the pulse option on the AN-1003 anemometer, which produced a wave from 0-10 volts for 2 μs on the specified channel. The voltage pulse through the hotwire element creates a second order output, where the frequency response can be calculated graphically. The voltage was set to $\approx$ 5 volts for all experiments. A potentiometer on the each channel changes the damping coefficient within the Wheatstone bridge. Over-damping the bridge results in only a single peak, while under-damping results in unstable oscillations. The damping was adjusted until the output resembled the optimum square wave test response (critically damped) and the frequency response was calculated as shown in figure 2-15. The laminar jet velocity of the calibration nozzle was set to the maximum experimental velocity used (10 m/s) during a square wave test. This ensures that during the test the hotwire encounters frequencies close to the highest in the actual experiments, and that the minimum frequency response time is calculated. Subsequent lower velocities will produce a higher frequency response, these are not measured.

After performing the square wave test on each channel, a calibration sequence was run. The calibration process for the vorticity probe is explained in section 2.3. After calibration, the probe is gently moved (without disconnecting any cables) to into the tunnel test section and mounted on the traverse. The two frequency drives that run the blower motors are started and run for over 500 seconds before the tunnel test section velocities plateau. Due to the high volume flow rate of air moving through the test section, in comparison to the relatively low volume of the room, the dynamics in the room must reach a steady state before the velocity in the test section equilibrates. See figure 2-16

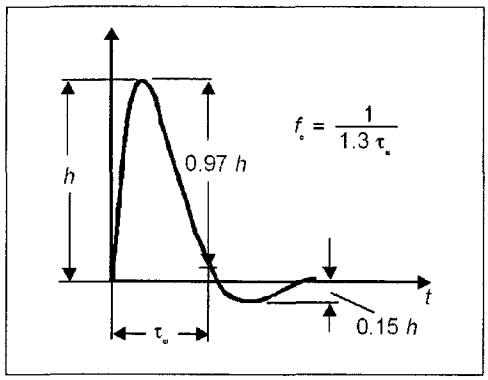

Figure 2-15: Optimum square wave test response, [1]

for a plot of test section velocities versus time.

Up to 8 wall normal profiles were taken at increasing streamwise distances from the separation edge. The streamwise locations are logarithmically spaced. such that profiles were closer together near the separation edge. The first five profiles were acquired within x=26mm of the separation edge, and the furthest profile was at x=343mm. Table 2.3 gives the streamwise locations for each of the profiles in millimeters and normalized by the momentum deficit thickness for the blunt and sharp edge. Due to the extended length of the sharp edge, the downstream distance was constricted by the length of the streamwise traverse. Thus, the sharp edge cases only reach a downstream distance of 216 mm.

At each of the streamwise locations, a coarse (whole field) and near-wall profile of 79 data points each were acquired. For consistency between the experiments using the blunt and sharp trailing edges, the wall normal origin was set at the center of the splitter plate. The whole field profile spanned a wall normal distance of 76 mm on each side of the wall normal origin. The near wall profile spanned a wall normal distance of 13 mm for the sharp edge and 19 mm for the blunt edge (see figure 2-17). The additional thickness of the blunt edge geometry required a slightly larger distance than the sharp edge. The data

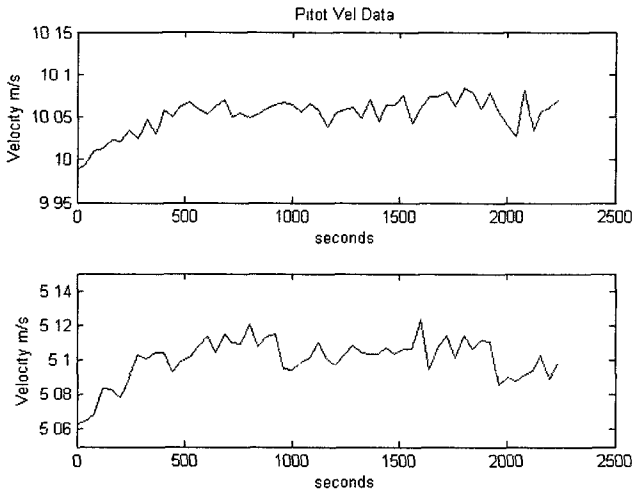

Figure 2-16: Pitot static velocity data during wind tunnel start up

Blunt Edge		Sharp Edge	
(x/θ)	(mm)	(x/θ)	(mm)
1.76	3.80	1.76	3.80
2.94	6.35	2.94	6.35
5.88	12.70	5.88	12.70
8.82	19.05	8.82	19.05
11.76	25.40	11.76	25.40
41.16	88.91	41.16	88.91
82.31	177.79	99.95	215.89
158.75	342.90	-	-

Table 2.3: Downstream profile locations for blunt and sharp edge

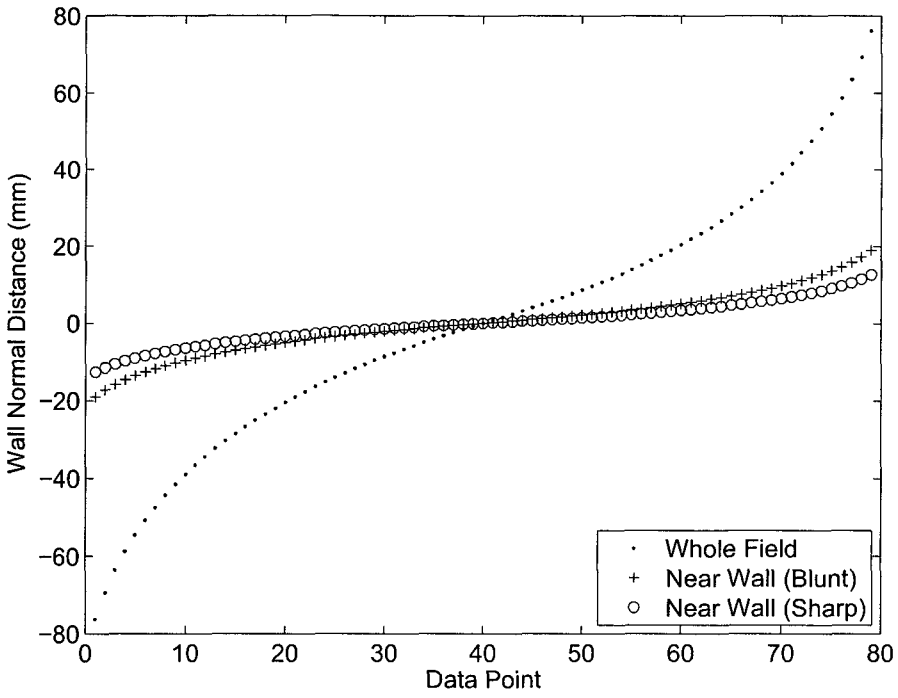

Figure 2-17: Wall normal distance (mm) vs data point number

point spacing in the wall normal profiles were logarithmic, such that there were more data points near the plane of the splitter plate, and fewer data points near the free stream. After a profile was acquired, the hotwire probe was removed from the test section and placed back in the calibration apparatus for the post experiment calibration. This was done to verify that unacceptable hotwire drift did not occur during the profile acquisition (see section 2.3).

Chapter 3

Results

The following chapter presents results from the four wire vorticity probe for three different cases. The first two cases utilized the sharp trailing edge, one with shear (denoted as "SS", "Sharp Shear") and one without a net shear (denoted as "SNS", "Sharp No Shear"). The third case utilized the blunt trailing edge with shear (denoted as "BS","Blunt Shear"). The shear studies investigated the convergence of two separate wall bounded flows with a velocity ratio of 2:1 (10 m/s and 5m/s). The case without a net shear largely represents a reference case, as it examines the convergence of two separate wall bounded flows with the same velocity (10 m/s), but still containing opposing signs of vorticity.

The effects on the boundary layer flow separating at the trailing edge were of particular interest. In order to investigate this, the shear wake data acquired closest to the point of separation ($x/\theta = 1.76$), were compared to turbulent boundary layer data at roughly the same δ^+ values. This turbulent boundary layer data comes from a direct numerical simulation performed by Schlatter et al. [19]. In this comparison mean streamwise velocity and gradient, and velocity intensities were examined.

To better understand the evolution of a turbulent shear wake flow under these conditions, many characteristics were investigated including: the normalized mean streamwise velocity and its two derivatives, Reynolds stress and gradient, normalized fluctuating velocities, turbulence correlation coefficients, and others. These plots all utilize the scaled cross stream coordinate system $\eta = y/\delta_{sw}$ (described in section 2.4.5). For the SNS and SS case, $\eta = 0$ corresponds to the edge of the sharp plate. For the BS case, $\eta = 0$

corresponds to the center of the blunt plate, which extends to a wall normal distance of $-0.1 \leq \eta \leq 0.1$. For BS figures close to the point of separation, the splitter plate wall is denoted by vertical dashed lines. In each case, velocities are normalized by the friction velocity on the high speed side.

In order to clearly illustrate the characteristics of the flow evolution, some cases are plotted in two separate figures: post-separation region only ($x/\theta \leq 8.82$, and $-0.1 \leq \eta \leq 0.1$), and entire flow field ($x/\theta \geq 0$, and $-0.8 \leq \eta \leq 0.8$). Note that the figures showing blunt edge data sometimes have a slightly larger η domain in order to accommodate for the finite thickness of the splitter plate at the trailing edge.

The evolution of the viscous stress gradient ($\partial^2 U^+/\partial y^{2+}$) and the Reynolds stress gradient ($\partial \overline{uv}^+/\partial y^+$) are presented here for investigating the mean momentum balance (terms B and C, respectively in the mean momentum equation (1.7)). The primary region of interest for the mean momentum balance is in the vicinity of separation ($x/\theta \leq 10$). For this reason, it is applicable for the wall normal distance to be normalized using boundary layer properties (U_τ and ν) instead of shear wake properties (δ_{sw}) as before.

3.0.1 Upstream Boundary Layer Properties

Initial studies were performed using a single wire probe in order to estimate key experimental parameters such as sampling rate, turbulence frequency, upstream flow properties, and approximate downstream distance that the mixing layer occurred. These results were then used to help design the later tests with the vorticity probe. Boundary layer properties at the point of separation such as momentum and mass deficit thicknesses, skin friction coefficients, and shear wake width were also calculated from the single wire data.

In table 3.1, the upstream boundary layer properties are listed for both flow velocities. For all of the experiments the freestream velocities on the opposing sides of the splitter plate were kept within $\pm 3\%$ of their target values, 5 m/s or 10 m/s. Since each profile

Table 3.1: Upstream Boundary Layer Properties

Tunnel Side	U_∞ ($\frac{m}{s}$)	δ_{99} (mm)	$\%U_\infty$ Attained	δ^* (mm)	δ^+	Θ (mm)	Re_Θ	H ($\frac{\delta^*}{\Theta}$)
Low Speed	≈ 5	20.36	98.74%	2.04	312.18	1.70	583.66	1.203
High Speed	≈ 10	18.70	98.48%	2.83	539.8	2.16	1394.03	1.311

was acquired at discrete wall normal locations, the percentage the free stream velocity reached at wall normal distance δ_{99} was checked to insure it was near 99%. As seen in column 4 of table 3.1, this value was very close to 99%. As stated in previous sections, the momentum deficit thickness on the high velocity side ($\theta = 2.16mm$) was used to normalize all downstream distances. The δ^+ values were 569 and 367 for the high and low speed flows, respectively. It is important to note that the low speed flow is barely in the "four layer regime" due to its low δ^+ value. According to a study by Klewicki et al. (2011), the four layer regime depicted in figure 1-4 first becomes established at $\delta^+ \simeq 360$ [11].

3.1 Turbulent Boundary Layer Comparison

Very close to the point of separation, the shear wake flow contains many of the characteristics present in the turbulent boundary layer flow upstream. The mean profiles that were acquired closest to the plate ($x/\theta = 1.76$), were compared against high and low velocity, turbulent boundary layer data at $\delta^+ \simeq 660$ and 360. These mean profiles are derived from the direct numerical simulation performed by Schlatter et al. [19].

All mean profiles were normalized using the friction velocity (u_τ) and kinematic viscosity (ν). The five friction velocities were roughly calculated using the Clauser plot method

Table 3.2: Friction Velocities for all Experiments at $x/\theta = 1.76$

	u_τ (m/s)	
Experiment	10 m/s	5 m/s
Sharp No Shear	0.419	-
Sharp Shear	0.442	0.229
Blunt Shear	0.433	0.229

described in section 2.4.5. After which, the values were slightly adjusted to such that the freestream velocity (U^+) of the shear wake data matched the normalized freestream velocity of the DNS data. This was done to approximate a comparison with the boundary layers prior to the wall divergence associated with the formation of the sharp edge geometry. Note, however, that the boundary layers clearly exhibit the effect of the adverse pressure gradient cause by this divergence. Overall, it is seen that the separating boundary layers are significantly distorted compared to the canonical flow. In the SS case this seems to be cause by the short region of adverse pressure gradient cause by the wall divergence. In the BS case the likely mechanism is speculated to be associated with a feedback between the separation bubble and the upstream boundary layer. In either case, there is a more dramatic effect on the low speed stream. All friction velocity values are listed in table 3.2. The mean profiles were plotted against wall normal distance, y^+. A semi-log, x-axis is employed for all but the mean velocity gradient. The figures from the high speed flow present the DNS data (dash-dot), SNS case ($\diamond$), SS case ($\circ$), and the BS case ($\square$). The figures from the low speed flow are the same, except there is not a SNS case with low speed flow.

Mean streamwise velocity for the high and low speed flows are presented in figures 3-1 and 3-2, respectively. In the high speed flow, the blunt edge type almost matches

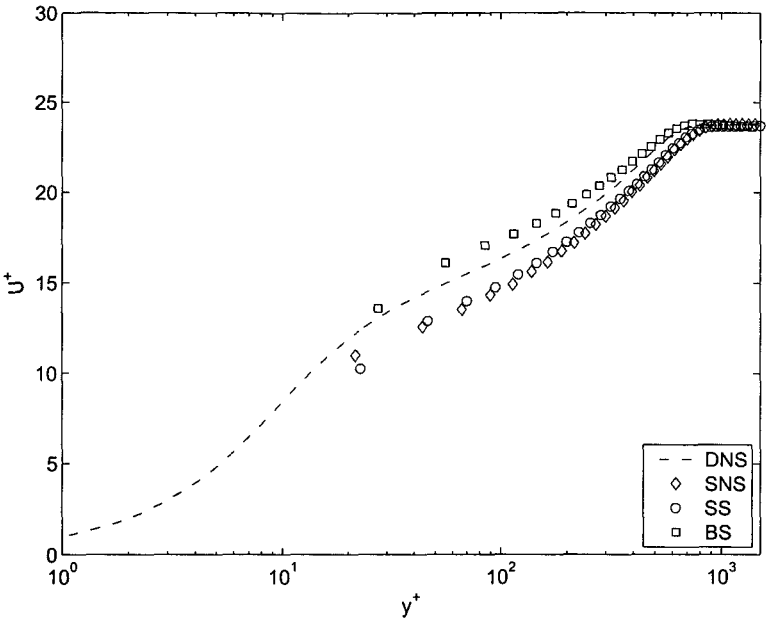

Figure 3-1: High speed flow U^+ for SNS, SS, BS, and turbulent boundary layer DNS data [19]

the DNS data, except for a small increase in U^+ near the wall. Both sharp cases display lower velocities than the DNS data for $y^+ < 500$. This difference can most likely be attributed to the pressure gradient created from the divergence of the wall in the sharp edge geometry. In the low speed flow, the slope of the logarithmic region in the BS case is seen to be less steep than the DNS data. The SS case displays the same lower, near wall velocities as the high speed, sharp edge profiles.

Mean streamwise velocity gradient ($\partial U^+/\partial y^+$) for the high and low speed flows are shown in figures 3-3 and 3-4, respectively. In the high speed flow, all exhibit good agreement with the DNS turbulent boundary layer data for all y^+. Consistent with the mean velocity profiles, the low speed flow shear wake data are slightly more scattered for $y^+ < 500$ than the high speed data. It is apparent however, that the outer region mean vorticity distribution in the nascent shear-wake is very much like that of the boundary layer.

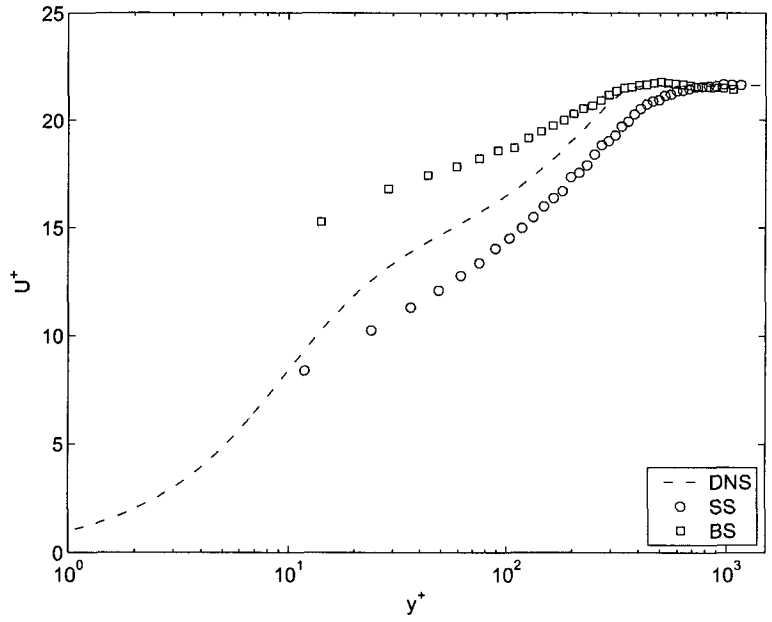

Figure 3-2: Low speed flow U^+ for SS, BS, and turbulent boundary layer DNS data [19]

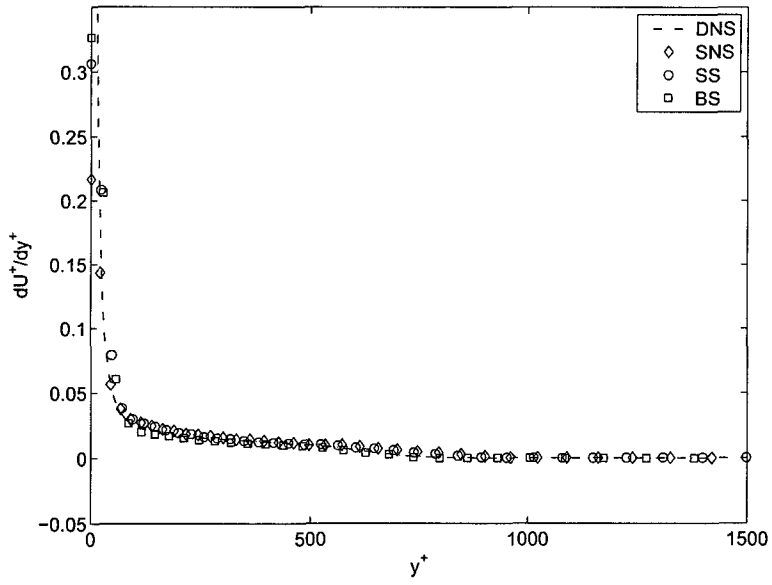

Figure 3-3: High speed flow $\partial U^+/\partial y^+$ for SNS, SS, BS, and turbulent boundary layer DNS data [19]

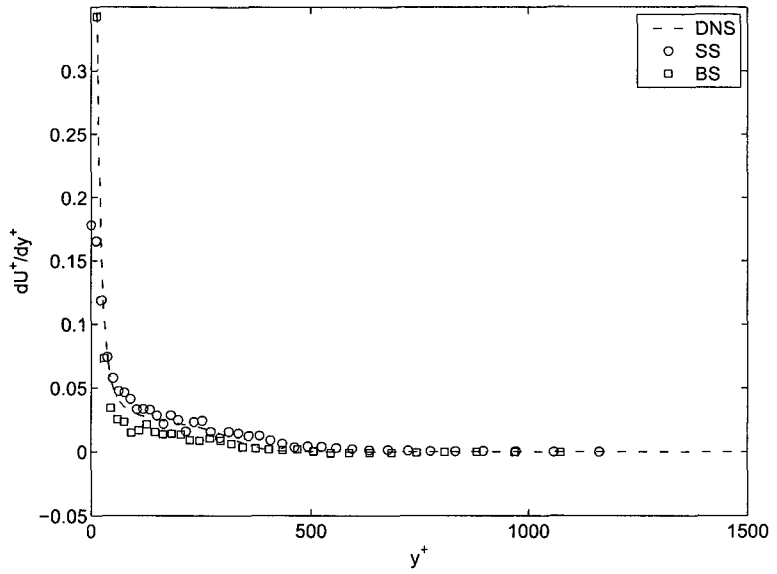

Figure 3-4: Low speed flow $\partial U^+/\partial y^+$ for SS, BS, and turbulent boundary layer DNS data [19]

The normalized streamwise velocity intensities (u^+_{RMS}) for the high and low speed flows are presented in figures 3-5 and 3-6, respectively. The agreement between the BS case and DNS data in the high speed flow is seen to be very close for all y^+ where shear wake data were acquired. Close to the wall ($y^+ < 500$), in the SNS and SS case the fluctuating velocities are slightly higher than that of the turbulent boundary layer DNS data. Again, this is mostly likely attributable to the diverging wall in the sharp edge geometry. In the low speed flow, the BS case tracks with the DNS data better than the SS case. An increase in u^+_{RMS} values is observed for all wall normal distances in the SS case.

The normalized wall normal velocity intensities (v^+_{RMS}) for the high and low speed flows are presented in figures 3-7 and 3-8, respectively. In the high speed flow, the peak values near $y^+ \simeq 100$ are slightly higher in the sharp edge cases than the DNS data, while the BS case is slightly lower than the DNS data. Overall, the three v^+_{RMS} profiles are seen

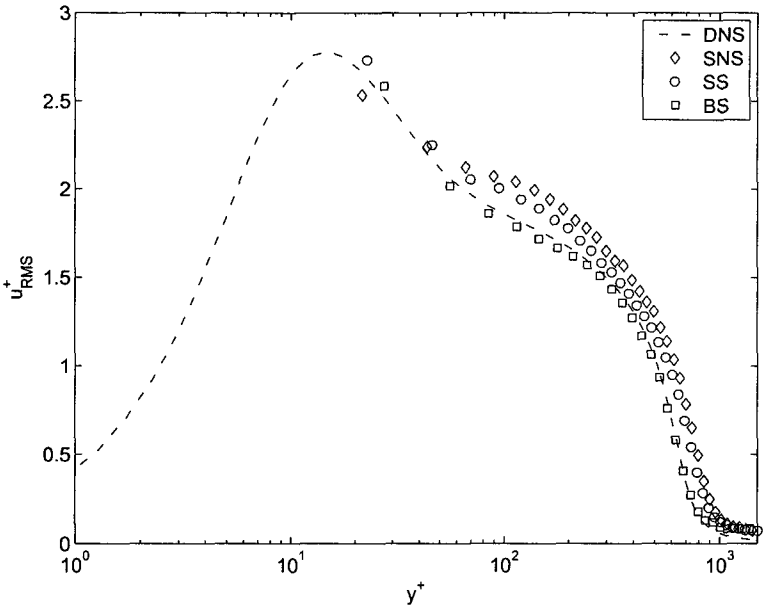

Figure 3-5: High speed flow u^+_{RMS} for SNS, SS, BS, and turbulent boundary layer DNS data [19]

to trend fairly well with the turbulent boundary layer data. The BS case in the low speed flow matches the curvature of the DNS data very well. While the SS case displays slightly higher velocities for all wall normal distances. This is consistent with the presence of the short region of adverse pressure gradient caused by the diverging wall associated with the sharp trailing edge.

3.2 Mean Steamwise Velocity & its Derivatives

Normalized mean velocity profiles were also acquired using the four element vorticity probe described in section 2.2.2. For all three studies the streamwise velocity data was normalized by the friction velocity from the high speed flow with the blunt edge ($u_\tau = 0.433m/s$). Likewise, the wall normal distances were normalized by the shear width ($\delta_{sw}(x)$) calculated at each individual downstream position. In these figures, recall that

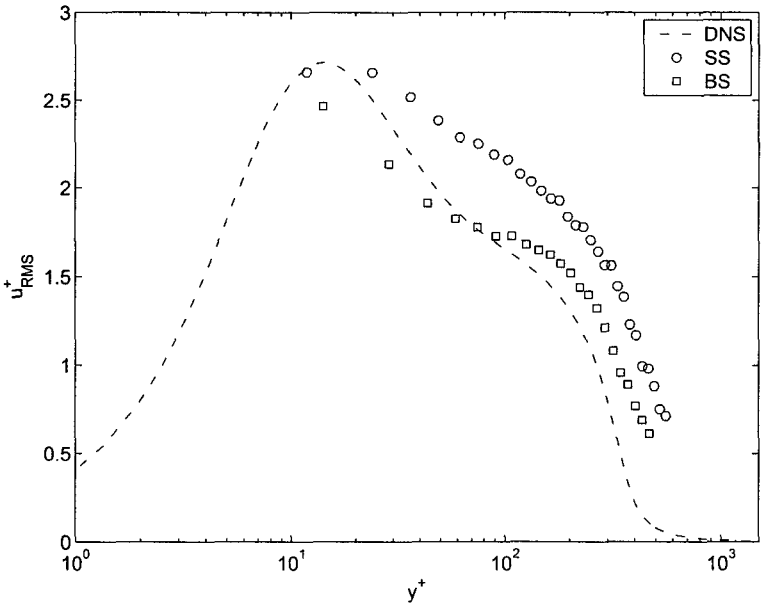

Figure 3-6: Low speed flow u^+_{RMS} for SS, BS, and turbulent boundary layer DNS data [19]

the thickness of the splitter plate in the blunt edge study is located between $-0.1 < \eta < 0.1$ (denoted by the vertical dashed lines).

3.2.1 Mean Velocity (U^+)

As expected. the mean streamwise velocity profile in the SNS experiment (figure 3-9) exhibits a symmetric evolution about $y/\delta_{sw} = 0$ for all x/θ. At $x/\theta = 1.76$, two distinct boundary layers are apparent, with equal magnitude on each side of the sharp edge. The profiles up to a downstream distance of $x/\theta = 8.82$ all exhibit a maximum momentum deficit at $\eta = 0$. Further downstream, until at $x/\theta = 99.95$, the momentum deficit continues to diminish. In this case however, the existence of opposing signs of mean vorticity is still visible at the furthest downstream position. The downstream distance needed for the momentum deficit region to diminish entirely (having zero vorticity), is

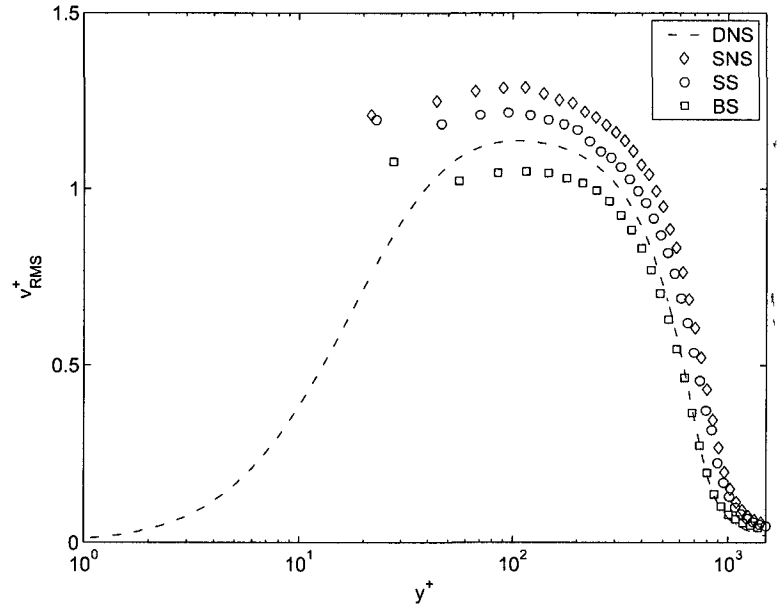

Figure 3-7: High speed flow v^+_{RMS} for SNS, SS, BS, and turbulent boundary layer DNS data [19]

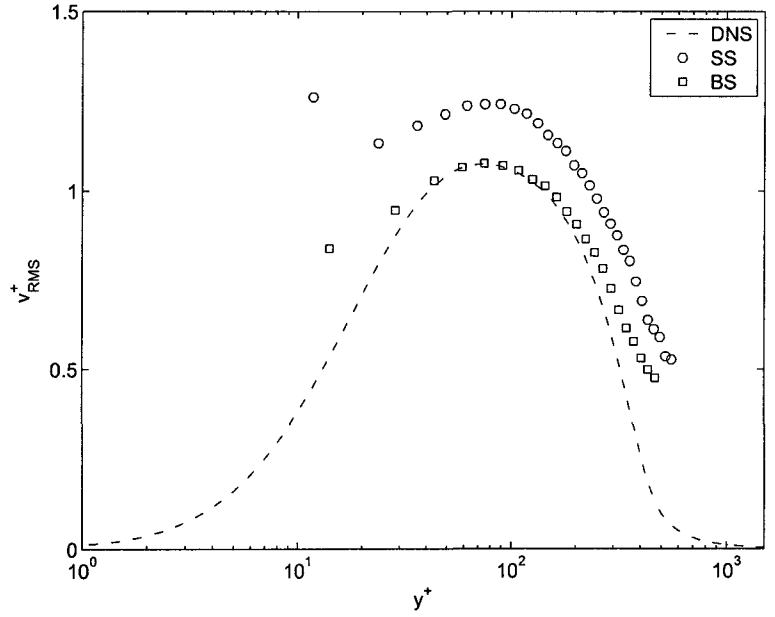

Figure 3-8: Low speed flow v^+_{RMS} for SS, BS, and turbulent boundary layer DNS data [19]

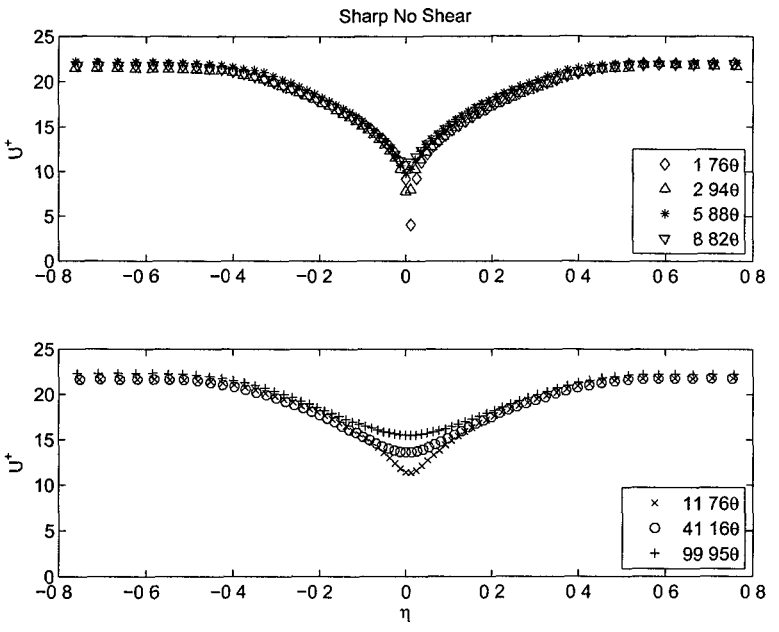

Figure 3-9: Normalized Mean Streamwise Velocity with increasing x/θ for SNS case

apparently much greater than the streamwise probe traverse would allow. According to figure 3-12, if the linear region shown continues for further downstream distances, the wake component would disappear for the SNS case around $x/\theta \simeq 1400$. However, the most of the streamwise velocity evolution can be seen for $x/\theta \leq 100$.

The SS and BS mean profiles (figure 3-10 and 3-11), exhibit similar behavior. Owing, however, to the sharp edge geometry, the abrupt momentum deficit region directly behind the plate of the BS experiment is not seen. At $x/\theta = 1.76$, two separate boundary layers are visible where one side has twice the magnitude as the other. These profiles remain quantitatively similar for a downstream distance of $x/\theta = 8.82$, where the small momentum deficit region directly behind the sharp edge is slowly filled in. By extrapolating the trend of figure 3-12, one can estimate that a free shear profile with one sign of vorticity should evolve by a downstream distance of 230θ.

The BS profiles of figure 3-11, at first ($x/\theta = 1.76$) show two distinct and separate

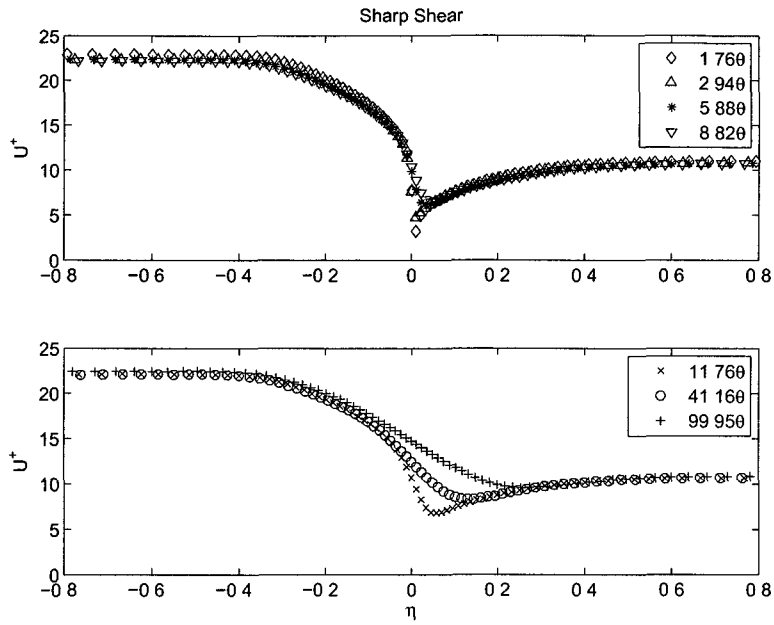

Figure 3-10: Normalized Mean Streamwise Velocity with increasing x/θ for SS case

boundary layers on each side of the splitter plate. Directly behind the splitter plate a low momentum region is formed, and the streamwise velocity is near zero. This is likely to be a recirculation region caused by the finite thickness of the splitter plate. Further downstream to $x/\theta = 8.82$, a very similar profile to upstream is seen. By $x/\theta = 11.76$, momentum has begun to fill the velocity deficient region (stagnant flow) caused by the splitter plate thickness. By this location the separate boundary layers of the shear wake flow are significantly distorted and are beginning to directly interact with each other. At $x/\theta = 41.16$, the wake component continues to diminish as the low momentum region is being filled in. The furthest profile downstream ($x/\theta = 158.75$) is very nearly a free shear flow containing a single sign of vorticity. Unfortunately, this distance was limited by the range of the streamwise traverse. Since the flow is now evolving much slower in the streamwise direction, a perfect free shear profile could require significantly more downstream distance Using figure 3-12 as in the previous experiments, a single-signed

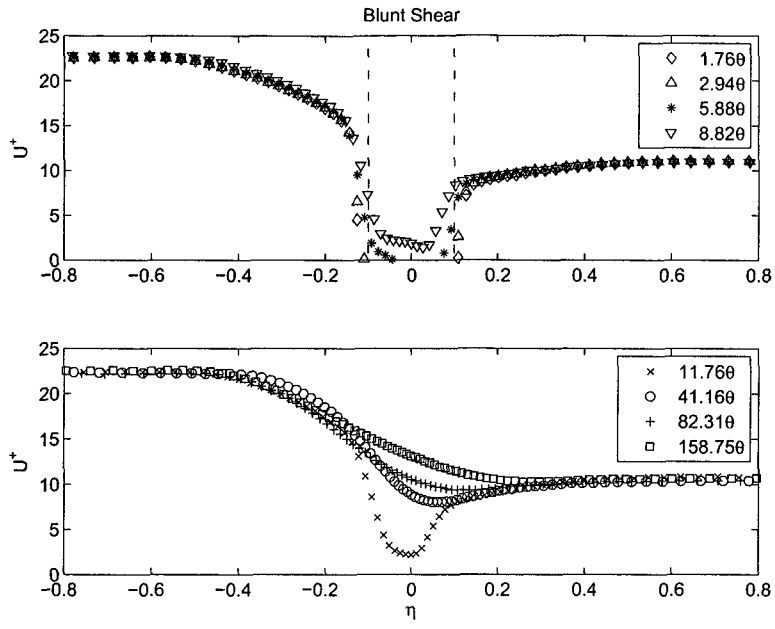

Figure 3-11: Normalized Mean Streamwise Velocity with increasing x/θ for BS case

profile is extrapolated to be realized at 200θ.

3.2.2 Wake Velocity Deficit

A measure of the rate of momentum transfer to the central portion of the wake is provided by quantifying the magnitude of the maximal wake deficit with streamwise position. Figure 3-12 shows the minimum streamwise velocity versus downstream location for the three flows under investigation. The streamwise velocity is normalized using the freestream velocity on the high speed side (U_∞) and is plotted on a log-log scale. For all experiments the minimum deficit velocity trends towards a slow power law for $x/\theta > 10$. Both shear cases have a slope near 0.15, while the no shear case has a slope of 0.13.

The location of the minimum velocity deficit relative to the surface of the splitter plate at $x/\theta = 0$ is plotted in figure 3-13. As expected for the case without shear, the location of the minimum velocity remains directly behind the plate at $\eta = 0$. In this case, the

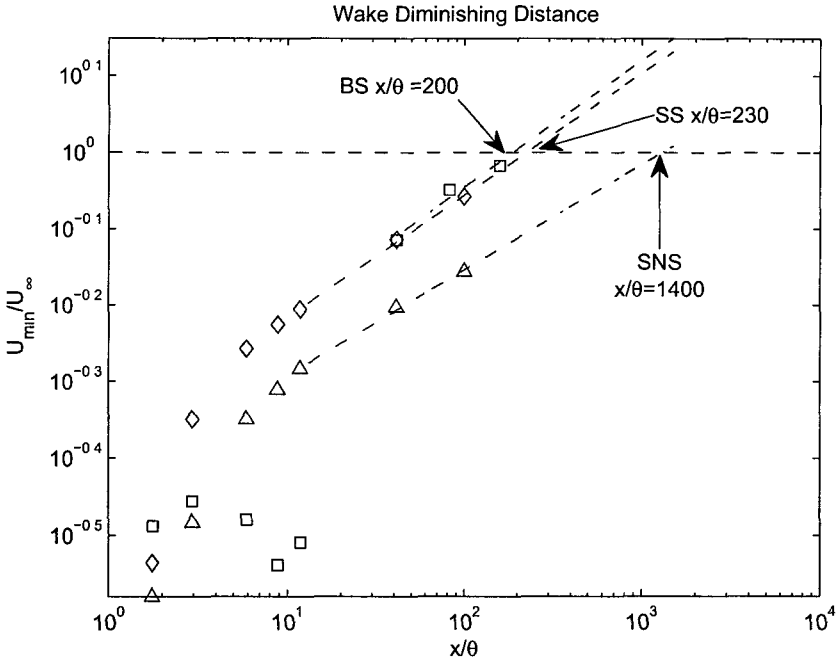

Figure 3-12: Projected downstream distance for free shear profile for SNS case (△), SS case (◇), and the BS case (□)

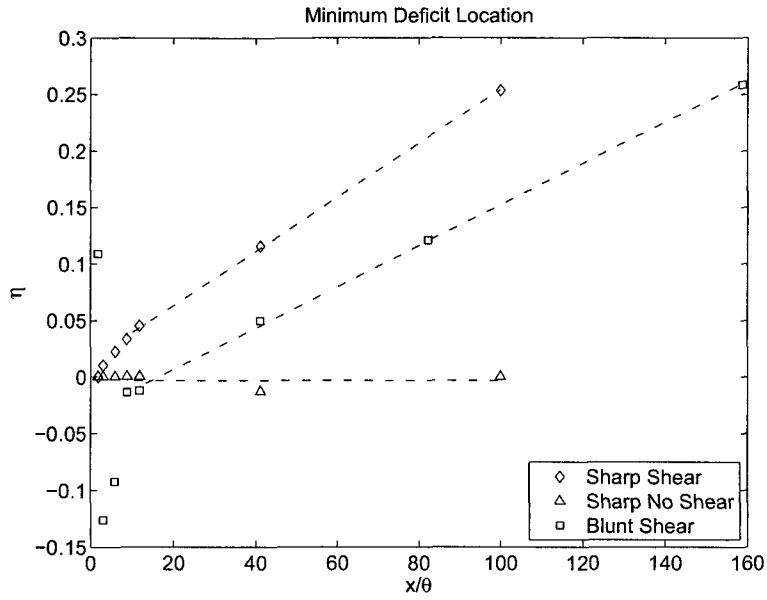

Figure 3-13: Wall Normal Location of Minimum Velocity Deficit

shear layers on either side of $\eta = 0$ are symmetric and contain the same distributions of mean momentum and mean vorticity. Thus, there is no mechanism to shift the minimum velocity point to one side of the plate. In the shear case there is a nearly linear shift of the wall normal location with respect to downstream distance when $x/\theta > 10$. This shift is towards the low speed side ($\eta > 0$). The more scattered locations of the deficit in the blunt case for $x/\theta < 10$ is due to the thickness of the splitter plate creating a wide region of low momentum, making it difficult to pinpoint an exact location of minimum velocity.

3.2.3 First Derivative of Mean Velocity

The mean velocity gradient was calculated with respect to wall normal coordinate η, and also plotted against η. For each gradient two figures are shown: first the near-field post separation region, and second the entire shear width domain and downstream distance. In

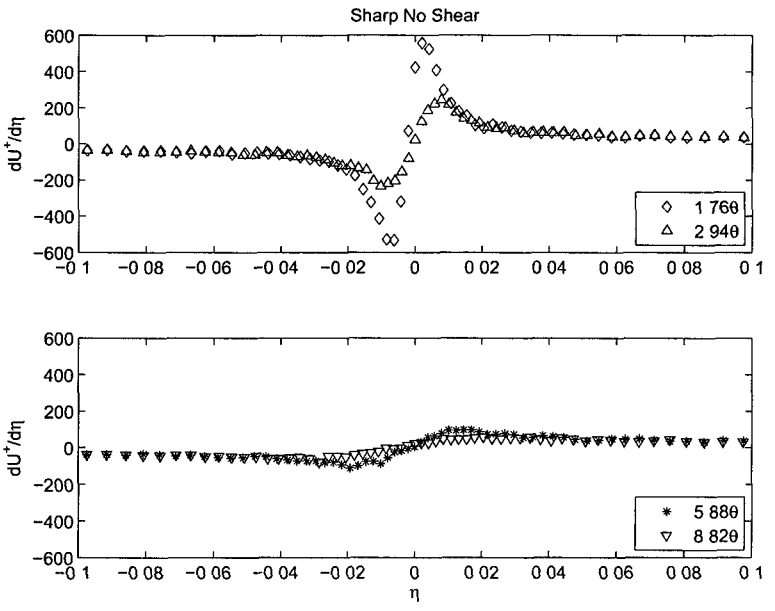

Figure 3-14: Normalized Mean Streamwise Velocity Gradient with increasing x/θ for SNS case (Post-Separation Region)

figures 3-15 and 3-14, the mean velocity gradient for the SNS experiment is shown. Close to the point of separation ($x/\theta \leq 8.82$), two symmetric peaks are seen with each reaching a magnitude near 600. Further downstream, the separate peaks become smoother, while decreasing in magnitude. The profile at maximal downstream location retains two slight peaks; however it is clear that these will continue to diminish downstream.

The mean velocity gradients for the sharp edge with shear case are shown in figures 3-16 and 3-17. Close to the point of separation ($x/\theta = 1.76$), the peak on the high speed side reaches a magnitude about three times larger than the case without shear. Immediately downstream, the magnitude of the peaks begin decrease, while increasing in width much like the no shear case.

The mean velocity gradients for the blunt edge with shear case are shown in figures 3-18 and 3-19. Close to the point of separation ($x/\theta = 1.76$), two peaks arise just outside

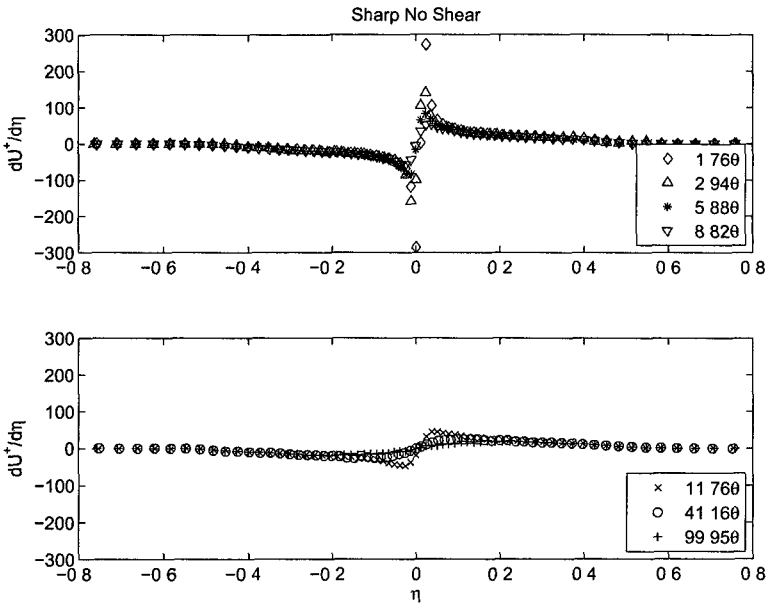

Figure 3-15: Normalized Mean Streamwise Velocity Gradient with increasing x/θ for SNS case

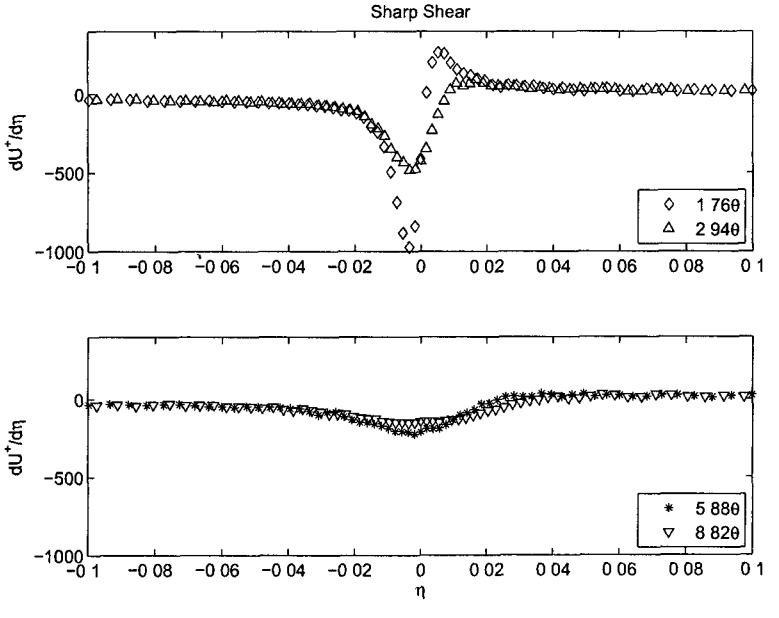

Figure 3-16: Normalized Mean Streamwise Velocity Gradient with increasing x/θ for SS case (Post-Separation Region)

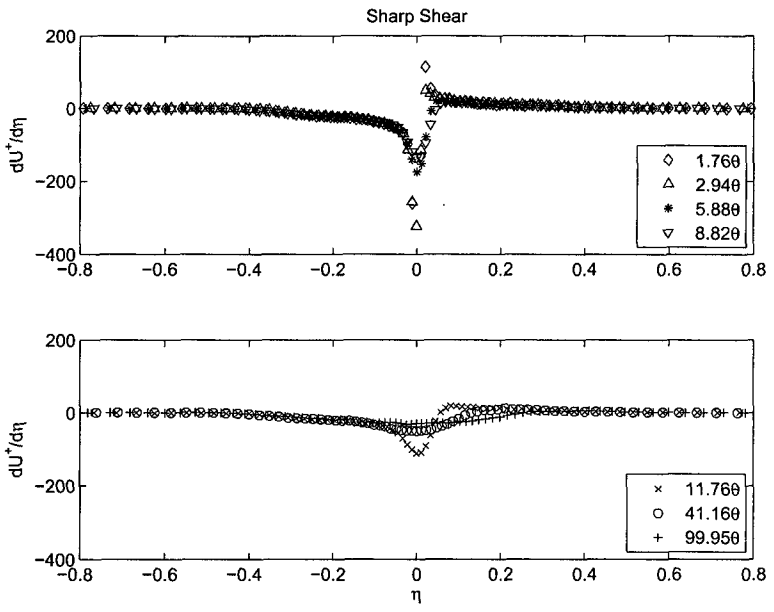

Figure 3-17: Normalized Mean Streamwise Velocity Gradient with increasing x/θ for SS case

of the splitter plate edges with the largest magnitude on the high speed side. As in the previous two cases, the peaks quickly decrease in magnitude and increase in width with downstream distance. In the blunt case however, the peaks on the low speed side shift inward with downstream distance. At the furthest location downstream, the peaks nearly disappear and a minimal amount of curvature seen behind the plate in the mean streamwise velocity gradient.

3.2.4 2nd Derivative of Mean Streamwise Velocity

In this section, the second derivative of the mean streamwise velocity with respect to wall normal coordinate η is presented. As discussed in the Introduction, this quantity is of central importance to momentum field development, as it effectively constitutes the mean viscous force in (1.7). Estimates for second derivative, $\frac{\partial^2 U}{\partial y^2}$, were found using by

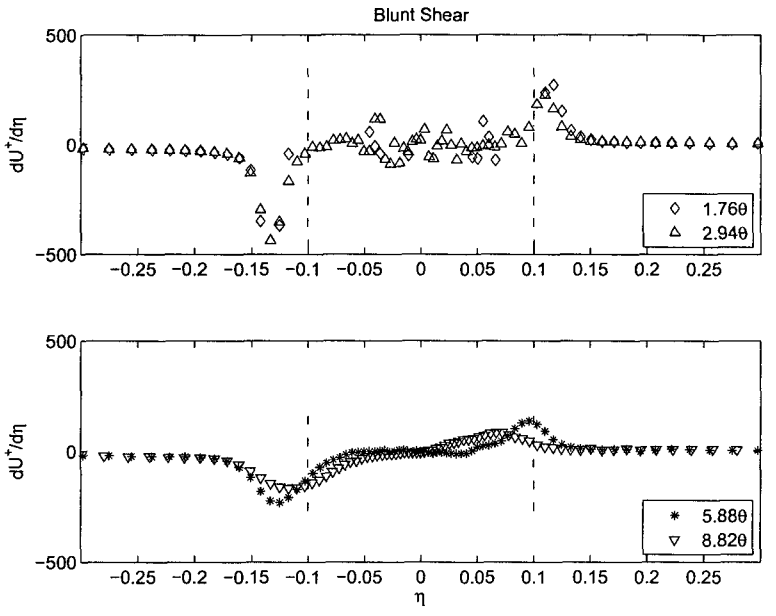

Figure 3-18: Normalized Mean Streamwise Velocity Gradient with increasing x/θ for BS case (Post-Separation Region)

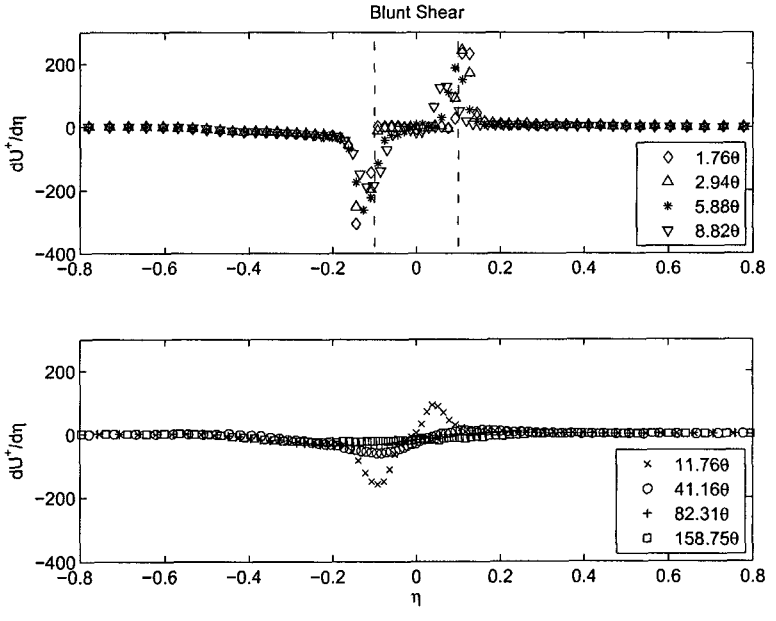

Figure 3-19: Normalized Mean Streamwise Velocity Gradient with increasing x/θ for BS case

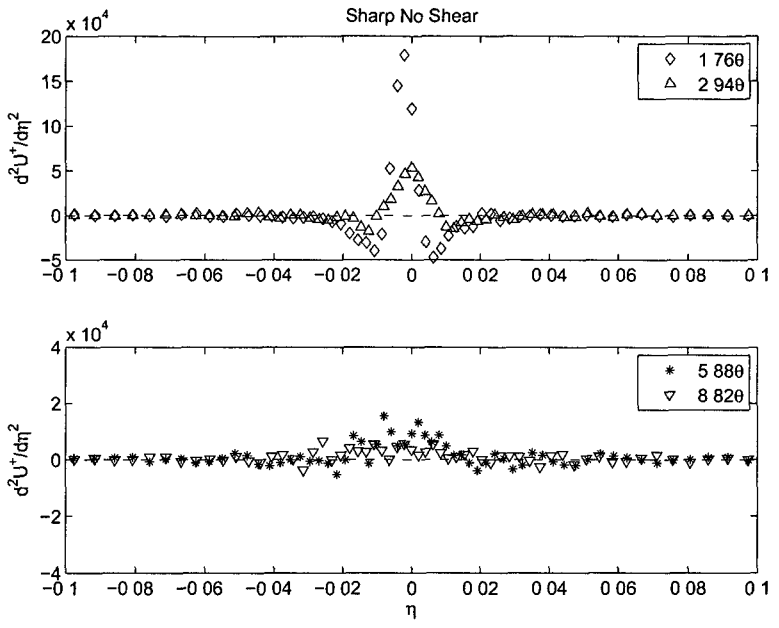

Figure 3-20: Viscous Force with increasing x/θ for SNS case (Post-Separation Region)

computing in these figures a central difference of streamwise velocity gradient shown in section 3.2.3. The resulting data for SNS, SS, and BS cases are shown in figures 3-20 - 3-25, respectively. The horizontal dashed line indicates the zero crossing of the profile, and thus indicates an inflection point in the velocity profile (i.e.. where curvature changes sign). The viscous force term was calculated as part of the mean momentum balance investigation.

Figures 3-20 and 3-21 plot the normalized viscous force profiles with respect to increasing downstream distance for the sharp edge without shear. The profiles closest to the separation edge in figure 3-20 show a distinct peak near $\eta = 0$. This peak significantly decreases in magnitude with increasing x/θ. On either side of the sharp edge ($\eta \approx \pm 0.1$) there are two negative peaks that only occur prominently at the first location ($x/\theta = 1.76$), but are still slightly visible at $x/\theta = 2.94$. Downstream of 2.94θ only a single positive peak is seen.

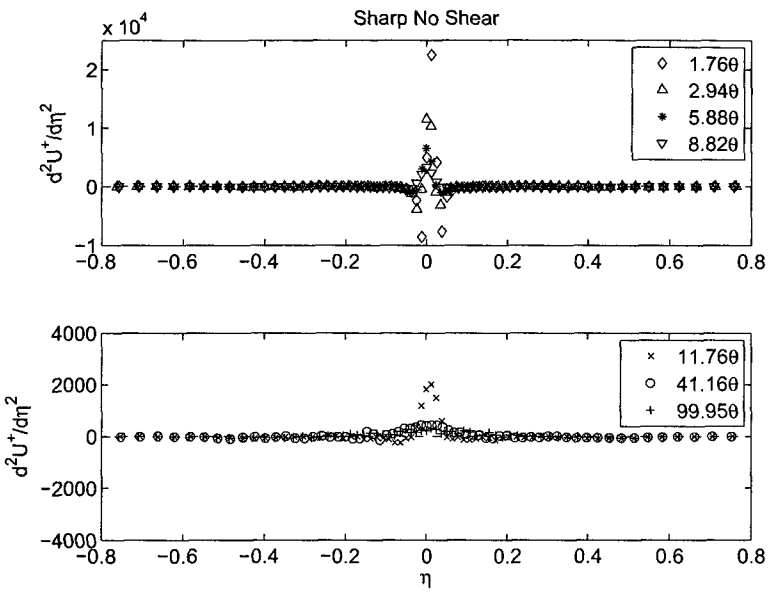

Figure 3-21: Viscous Force with increasing x/θ for SNS case

The viscous force profiles for the sharp edge with shear (figures 3-22 and 3-23) are similar to the case without shear. Near the edge ($x/\theta = 1.76$) a positive peak arises at $\eta = 0$, reaching approximately the same magnitude. On the either side of the splitter plate a negative peak is also formed, with larger magnitude on the high speed side. Downstream the peaks begin to decrease in magnitude and increase in width.

Figures 3-24 and 3-25 show the viscous force profile for the blunt edge with shear. The vertical dot-dashed lines denote the edge of the splitter plate walls. Very close to the edge ($x/\theta \leq 2.94$), negative peaks are seen on either side of the splitter plate. Directly behind the plate, the data becomes scattered as seen in the blunt edge velocity gradient (see figure 3-19). At $x/\theta = 5.88$, the profile becomes more continuous, still containing the negative peak just outside the wall and a positive peak interior. Also, the peaks in the low speed flow have shifted in slightly inwards. Downstream at $x/\theta = 11.76$, the same peaks are visible but show a decrease in magnitude. For greater x/θ the magnitudes of

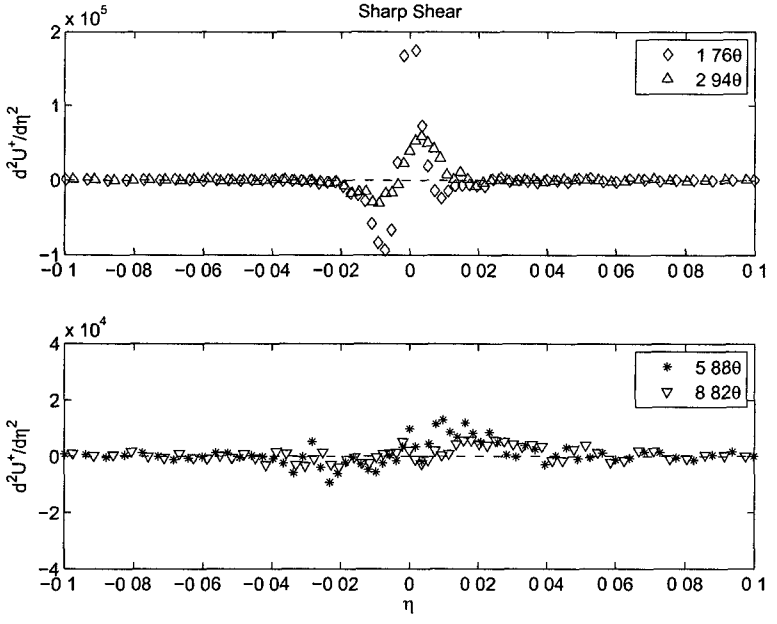

Figure 3-22: Viscous Force with increasing x/θ for SS case (Post-Separation Region)

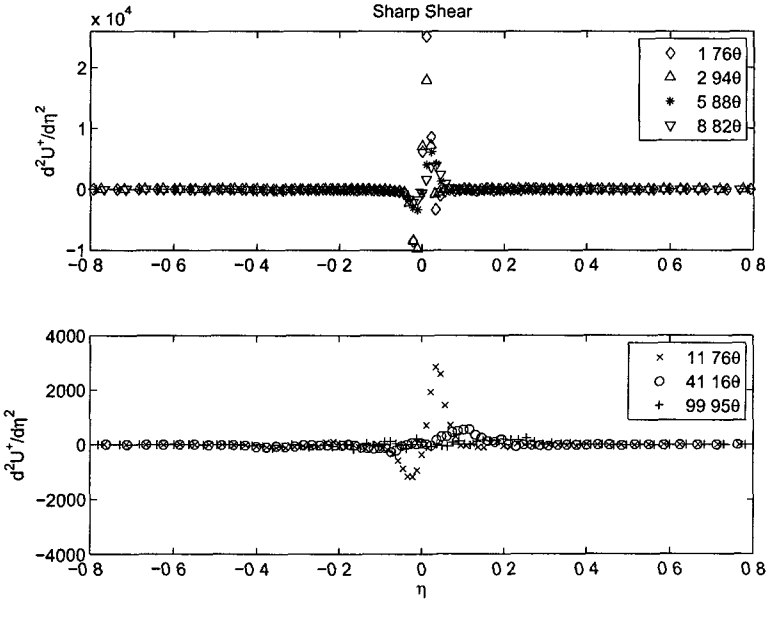

Figure 3-23: Viscous Force with increasing x/θ for SS case

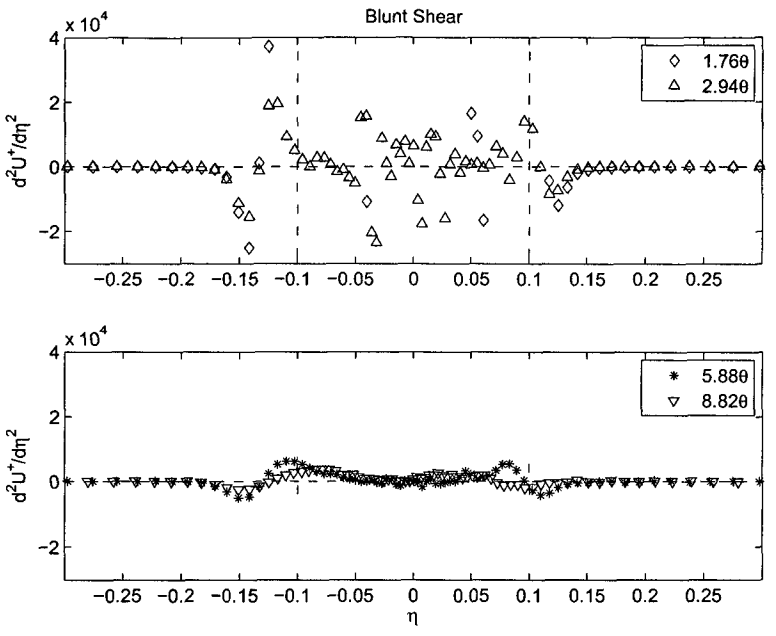

Figure 3-24: Viscous Force with increasing x/θ for BS case (Post-Separation Region)

the peaks significantly decrease and are hardly visible using the large y-axis range.

3.3 Reynolds Stress & its Derivatives

Reynolds stress profiles were acquired using the four wire vorticity probe, as described in section 2.2.2. The Reynolds stress data were normalized using the friction velocity ($u_\tau = 0.433m/s$) estimated for the high speed boundary layer. For this reason, the Reynolds stress peak on the low speed side of the plate reaches a peak value that is much less than unity.

The Reynolds stress profiles for the SNS experiment are shown in figure 3-26 for increasing x/θ. As expected, these profiles are symmetric profile about the center of the sharp edge at $\eta = 0$. Close to the separation edge ($x/\theta \leq 8.82$), the peaks on either side reach a value near unity with a steep "discontinuity" between. These magnitudes and

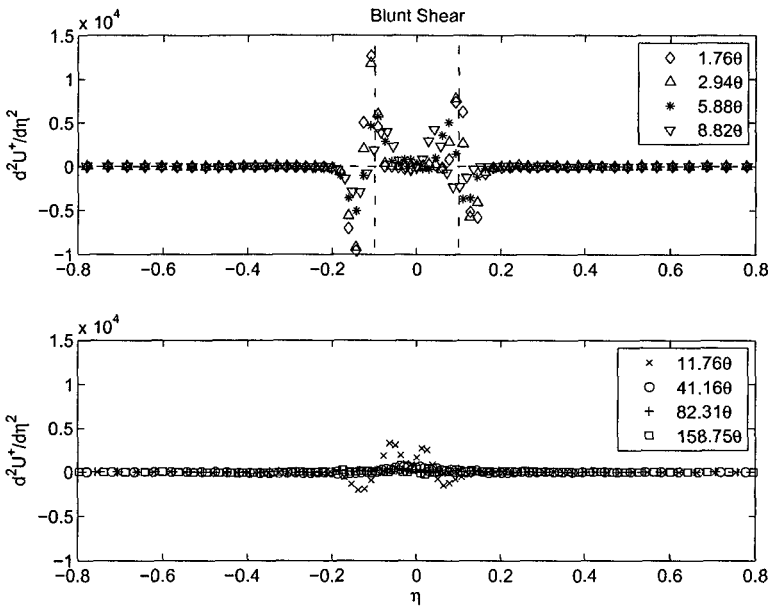

Figure 3-25: Viscous Force with increasing x/θ for BS case

shapes reflect the boundary layer-like characteristics of $< uv >^+$ for $x/\theta \lesssim 10$. Downstream, the peaks begin to move outward and decrease in magnitude, while increasing in width. At $x/\theta = 41.16$ a smooth curve is observed with two peaks at $\eta = \pm 0.1$. This trend continues to the furthest downstream location of $x/\theta = 99.95$.

The Reynolds stress profiles acquired for the SS case are shown in figure 3-27. The profile acquired closest to the separation edge exhibits two smooth opposing peaks on either side of the splitter plate, with the profile on the high speed side attaining a value near unity. Almost immediately, however a steep secondary peak near either side of the sharp edge is formed with a magnitude of about 1.5 (see profile at $x/\theta = 2.94$). The secondary peaks remain of constant magnitude downstream until $x/\theta = 8.82$. At $x/\theta = 11.76$ the largest secondary peak is seen at a wall normal location of $\eta = 0$. For greater downstream distances the peaks decrease in amplitude, and, as expected, broaden.

The Reynolds stress profiles acquired for the BS case are shown in figure 3-28 for

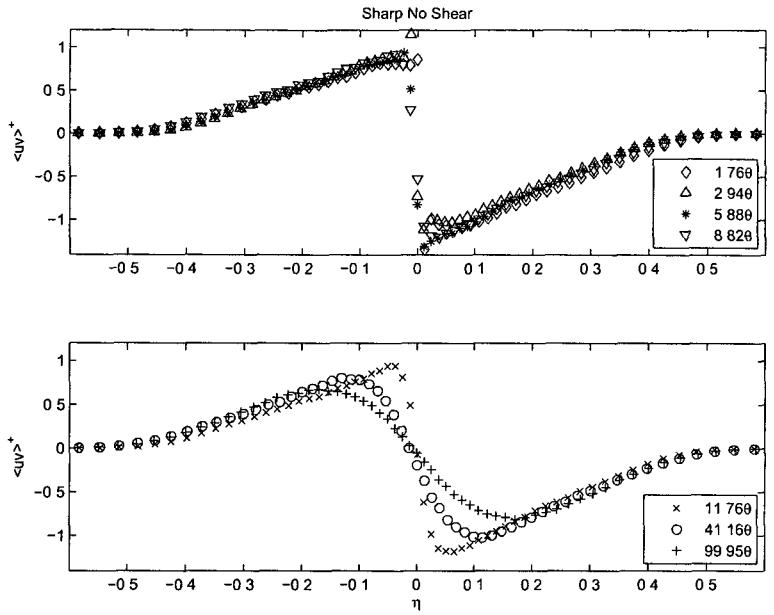

Figure 3-26: Reynolds stress with increaseing x/θ for SNS case

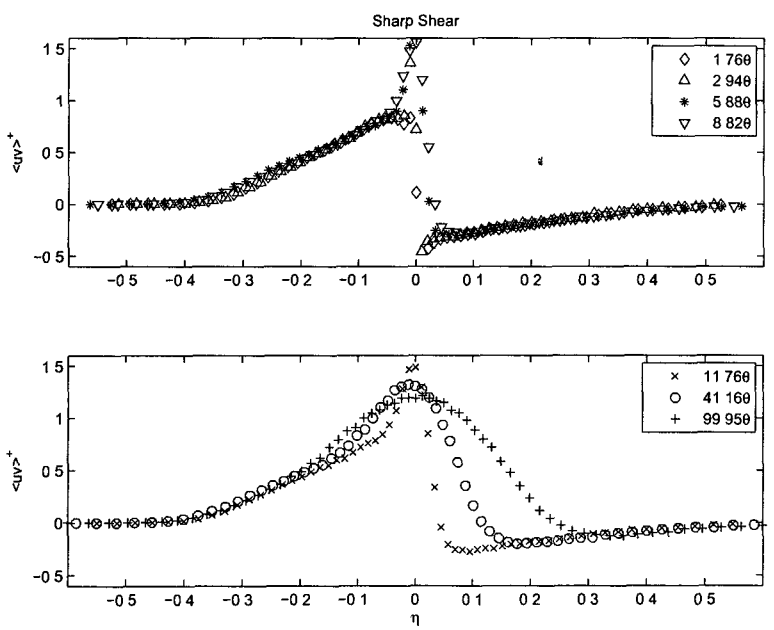

Figure 3-27: Reynolds stress with increaseing x/θ for SS case

increasing x/θ. The profiles closest to the separation edge ($x/\theta \leq 2.94$), exhibit smooth peaks of opposite signs that reach a magnitude near 0.6 on the high speed side and 0.2 on the low speed side. This is consistent with the absence of direct boundary layer interaction for $x/\theta = 0(1)$, owing to the finite width of the plate (about 6θ thick). In the inner region the data points become scattered and discontinuous, due to the significantly low momentum fluid directly behind the splitter plate edge. In this region the hotwire measurements lose reliability. At $x/\theta = 5.88$, a larger, secondary peak is seen right at the edge of the wall on the high speed side ($\eta = -0.12$). The secondary peak is shifted inward on the low speed side ($\eta = 0.07$).

Further downstream, at $x/\theta = 11.76$, the opposing sign secondary peaks are connected and an inflection point exists between them near $\eta = 0.03$. The highest Reynolds stress peaks are seen at this x/θ. In the last three downstream positions, the peaks begin to broaden, decrease in magnitude, and continually shift towards the high speed side. A constant magnitude and peak wall normal location is attained for x/θ of 82.31 and 158.75, but the profiles continue to increase in width.

The positions of maximum Reynolds stress as a function of x/θ in the high speed flow for all three cases are shown in figure 3-29. In the SNS case, the position of maximum $< uv >^+$ trends outwards from wall as x/θ increases. Close to the wall ($x/\theta = 1.76$), the y_m^+ value (peak distance from wall in y^+ units) is about 23. This compares quite well to turbulent boundary layer data at similar Reynolds number ($\delta^+ = 660$), where $y_m^+ \simeq 26$ [11]. When y_m^+ is plotted versus x/θ for the SNS case on log-log axis, a slope of roughly 0.87 is observed. In a turbulent boundary layer, when y_m^+ is plotted versus δ^+ on log-log axis, a slope of roughly 0.50 is seen [11]. These slopes are comparable due to the fact that δ^+ scales linearly with downstream distance, as does x/θ. In the SS case, the position of maximum $< uv >^+$ remains near $\eta \simeq 0$ for all x/θ. In the BS case, the horizontal dash-dot line indicates the wall of the blunt splitter plate. Near the separation

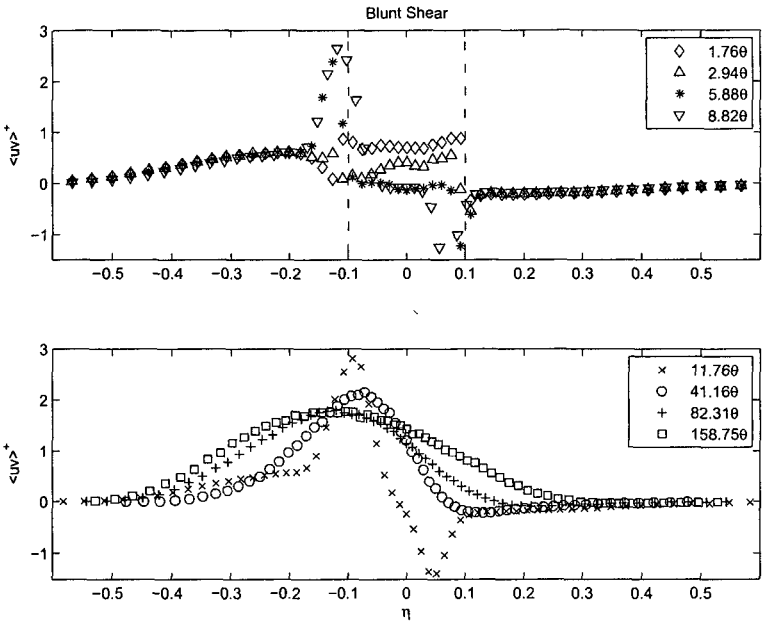

Figure 3-28: Reynolds stress with increaseing x/θ for BS case

edge ($x/\theta < 10$) the peak positions are scattered. However, downstream of 10θ, the peak positions remains near the edge of the wall at $\eta = -0.1$.

3.3.1 Reynolds Stress Gradient

Reynolds stress gradients, $\frac{\partial <uv>^+}{\partial \eta}$, were calculated by differentiating the normalized Reynolds stress with respect to wall normal coordinate η. The Reynolds stress gradient profiles for the SNS case are shown in figure 3-30. At a downstream distance of $x/\theta \leq 8.82$ a sharp negative peak is observed near $\eta = 0$. Downstream of the splitter plate edge, the negative peak continuously decreases while increasing in width. At the furthest downstream position only a slight peak is visible.

The Reynolds stress gradient for the SS case is seen in figure 3-31. One main difference between the shear and no shear case is the presence of a positive peak located on the high speed side. This peak occurs just before the wall ($\eta = -0.02$) and is seen for a downstream

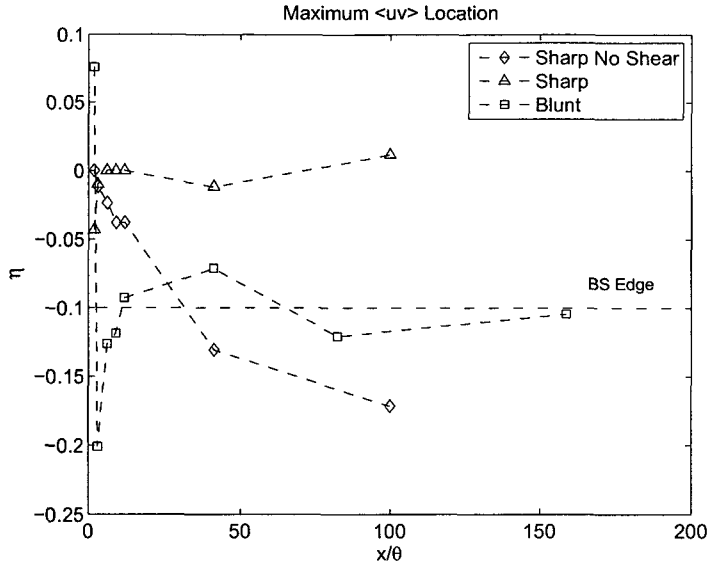

Figure 3-29: Position of peak Reynolds stress in high speed flow for SNS, SS, and BS cases

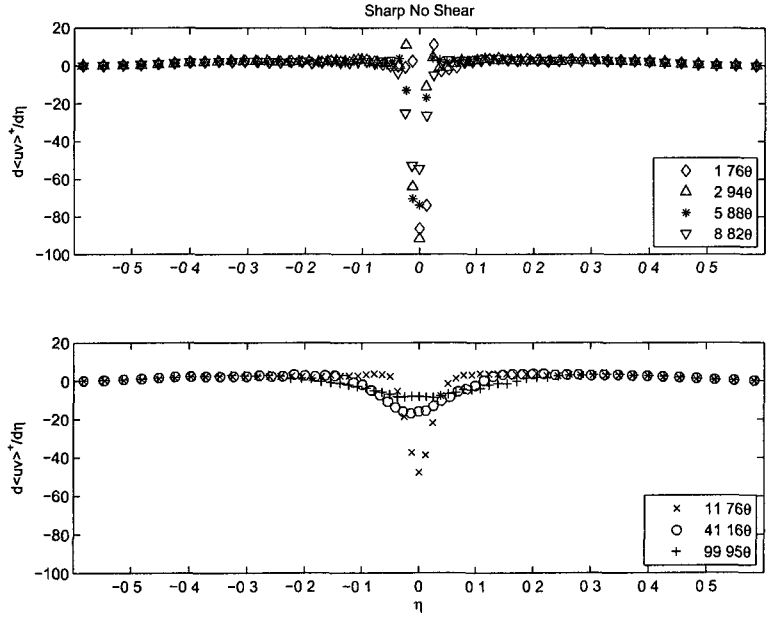

Figure 3-30: Reynolds Stress Gradient with increasing x/θ for SNS case

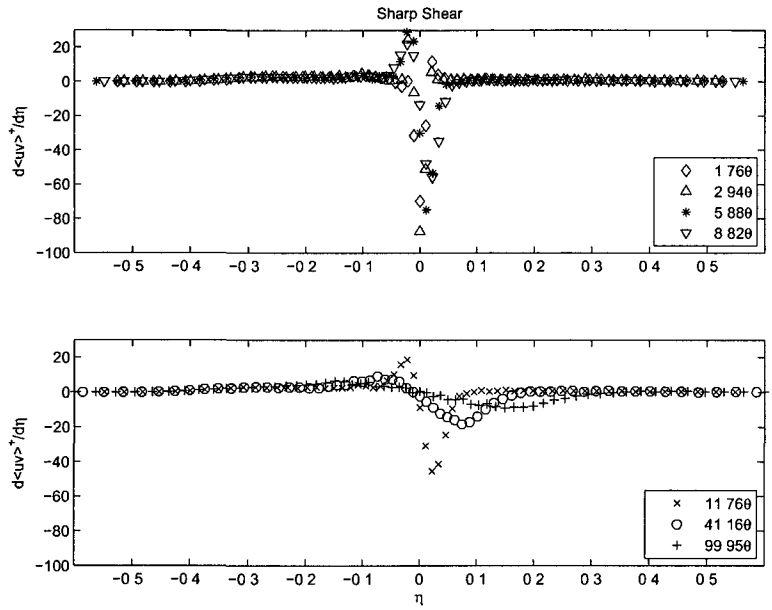

Figure 3-31: Reynolds Stress Gradient with increasing x/θ for SS case

distance of $x/\theta \leq 11.76$. A negative peak at $\eta = 0$ and $x\theta \leq 8.82$ is still observed, as in the no shear case. With the development of the mixing layer, the peaks begin to broaden and reduce in magnitude.

The Reynolds stress gradient for the BS case is shown in figure 3-32. As previously, the vertical dashed lines indicate the splitter plate wall. Close to the separation edge, positive peaks are seen near the splitter plate wall. Interior to the wall, two scattered, albeit identifiable, negative peaks occur. At $x/\theta = 11.76$, the two positive and two negative peaks are clearly evident. Downstream, the magnitudes rapidly decrease until a peak is scantly visible.

3.4 Velocity Intensities & Correlation Coefficients

The data acquired with the four wire vorticity probe were also used to compute the RMS streamwise and wall normal velocity profiles for both separation edge geometries. As

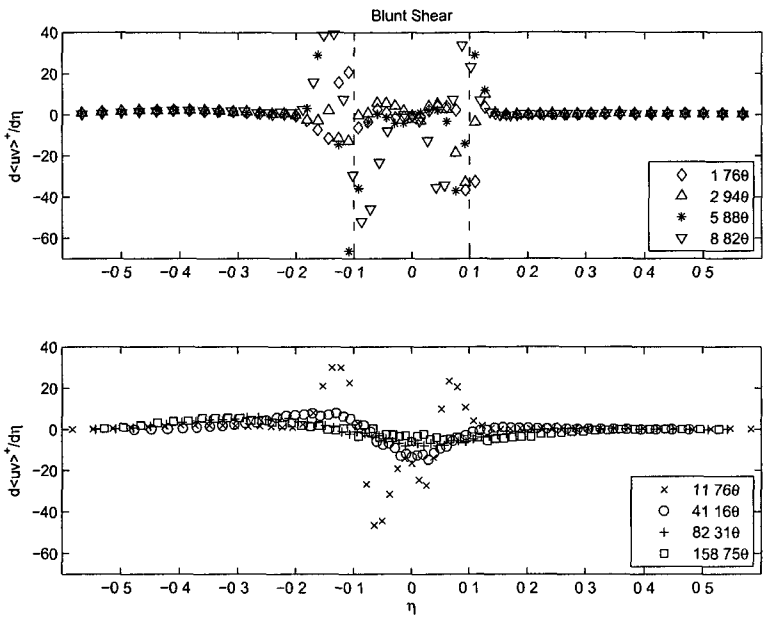

Figure 3-32: Reynolds Stress Gradient with increasing x/θ for BS case

previously stated, the RMS velocity was solved for using equation (2.7). Normalizations used the friction velocity (u_τ) from the high speed flow. The shear width at each respective downstream location is used to normalize the wall normal coordinate system (η) for both velocities.

3.4.1 RMS Streamwise Velocity (u_{RMS})

The u_{RMS} profiles for the sharp edge study without shear are shown in figure 3-33. For all downstream distances the profiles were symmetric about the sharp edge at $\eta = 0$. Close to the point of separation ($x/\theta \leq 8.82$), the normalized velocity intensity reaches a peak of about 2.5 at $\eta = 0$. This compares well with existing boundary layer data at the given Reynolds number, also see section 3.1. Moving towards either freestreams, the u_{RMS} values decrease until $\eta = \pm 0.6$. For $x/\theta > 8.82$ two peaks are seen on either side of the wall with a trough directly behind the sharp edge at $\eta = 0$. The peaks broaden and

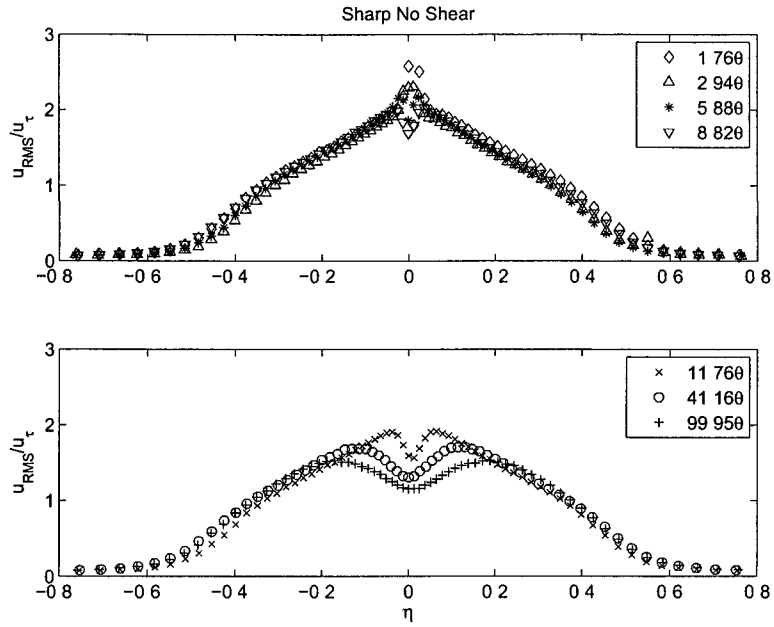

Figure 3-33: Fluctuating Streamwise Velocity with increasing x/θ for SNS case

move outwards as downstream distance increases. Outside of the center region of velocity deficit, all of the profiles approximately merge when plotted as a function of *eta*.

The normalized streamwise velocity intensity for the sharp edge with shear are shown in figure 3-34. For downstream positions $x/\theta \leq 8.82$ the high and low speed flow show similar characteristics but differ in magnitude The sharp peak at $\eta = 0$ has nearly the same magnitude as the sharp edge without shear case. The freestream u_{RMS} in the low speed flow remains higher than the high speed flow. As mention previously, this apparently is due to the fan blade buffeting at low RPMs Downstream the single peak begins to broaden while the magnitude stays relatively constant.

The streamwise velocity intensities in the blunt edge with shear flow are plotted in figure 3-35. Again, the vertical dashed lines denote the edge of the splitter plate. The first four profiles closest to the separation edge ($x/\theta \leq 8.82$) display high fluctuations near the wall while decreasing to zero away from the wall. In the high speed stream the peak of

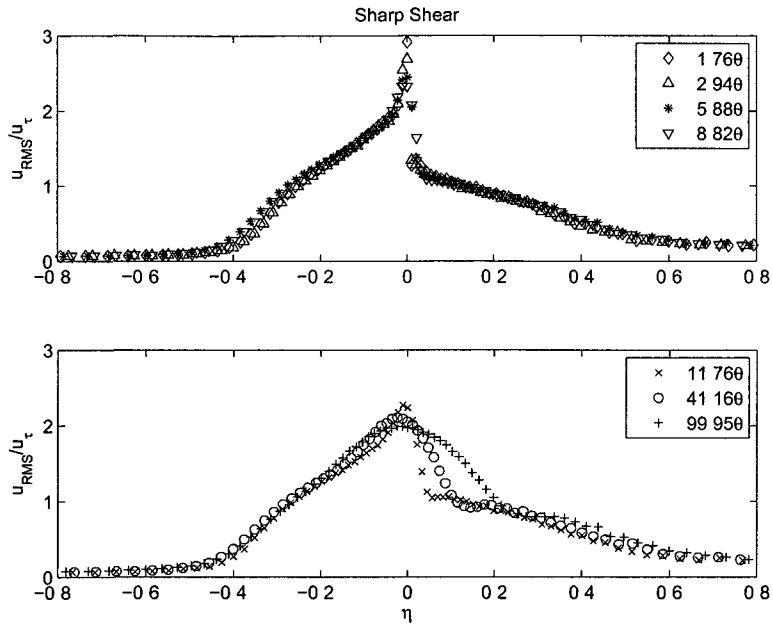

Figure 3-34: Fluctuating Streamwise Velocity with increasing x/θ for SS case

the fluctuations occur a small distance from the edge of the splitter plate, and decrease in either direction. This reinforces the fact that, very close to the separation edge, flow characteristics are similar to that of turbulent boundary layers. It is observed that the peak on the low speed side shifts inwards at further downstream positions. Behind the blunt splitter plate there is a distinct region, the width of the plate, containing smaller velocity fluctuations due to the momentum deficit at the point of separation.

At $x/\theta = 11.76$ the two separate peaks positioned slightly to the high speed side are still visible. At this streamwise distance, the largest intensities are seen (3.53 and 2.41 on the high and low speed side, respectively). Further downstream at $x/\theta = 41.16$, the RMS peaks are reduced into a single peak with lower magnitude. An increase in the width of the peak is also observed. Continuing downstream to $x/\theta = 158.75$, the magnitude of the peak remains near constant. The peak however, continues to broaden and move towards the high speed side.

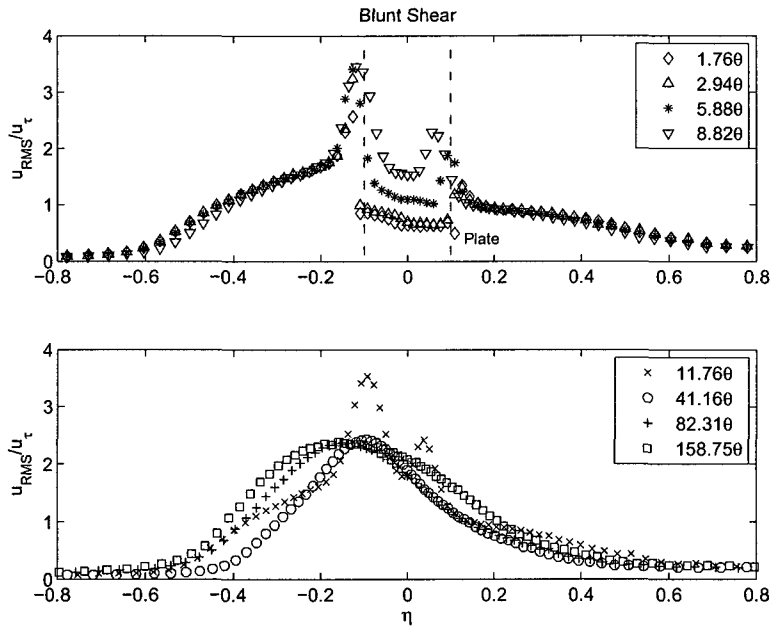

Figure 3-35: Fluctuating Streamwise Velocity with increasing x/θ for BS case

3.4.2 RMS Wall Normal Velocity (v_{RMS})

The wall normal velocity intensities for the sharp edge without shear case are given in figure 3-36. For all downstream distances, a smooth curve symmetric about $\eta = 0$ is observed. Close to the separation edge ($x/\theta \leq 11.76$) a small peak occurs at $\eta = 0$, which evolves into a slight trough further downstream. In both freestreams, the v_{RMS} values approach zero outside of $\eta = \pm 0.6$.

The v_{RMS} profiles for the sharp edge with shear study are shown in figure 3-37. For downstream distances $x/\theta \leq 8.82$, both flow velocities produce a similar profile but with differing magnitudes. A sharp peak at $\eta = 0$ is observed as in the case without shear. Similar to the u_{rms} profiles, the freestream values in the low speed flow do not approach zero as closely as the high speed does. Downstream of $x/\theta = 8.82$ the v_{RMS} profiles begin to evolve into a wider single peak at $\eta = 0$ with constant magnitude.

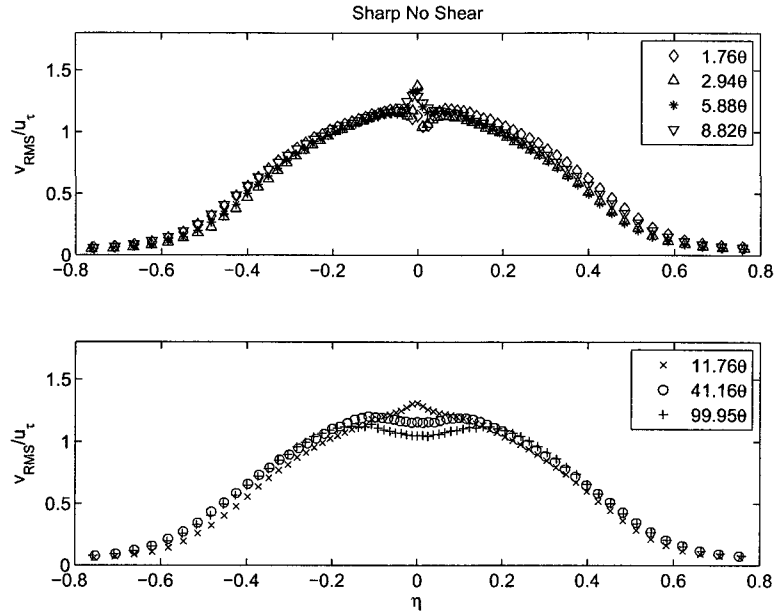

Figure 3-36: Fluctuating Wall Normal Velocity with increasing x/θ for SNS case

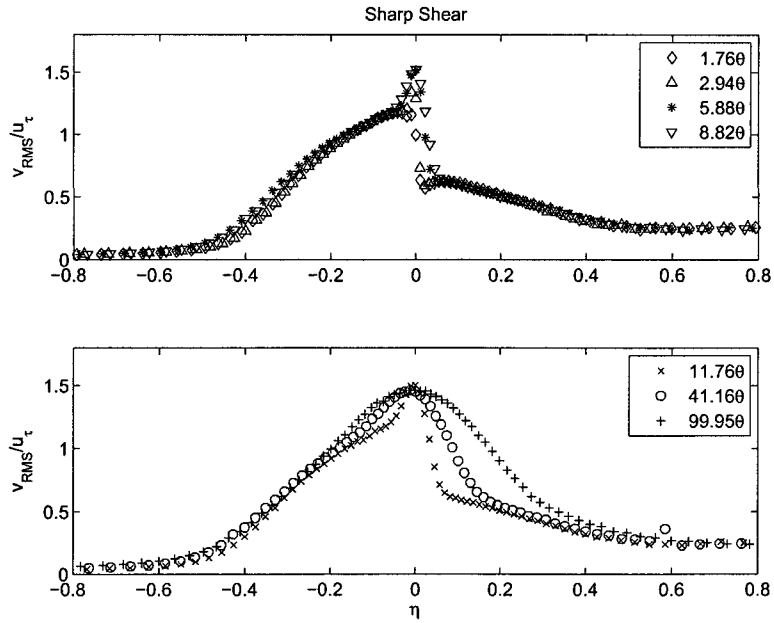

Figure 3-37: Fluctuating Wall Normal Velocity with increasing x/θ for SS case

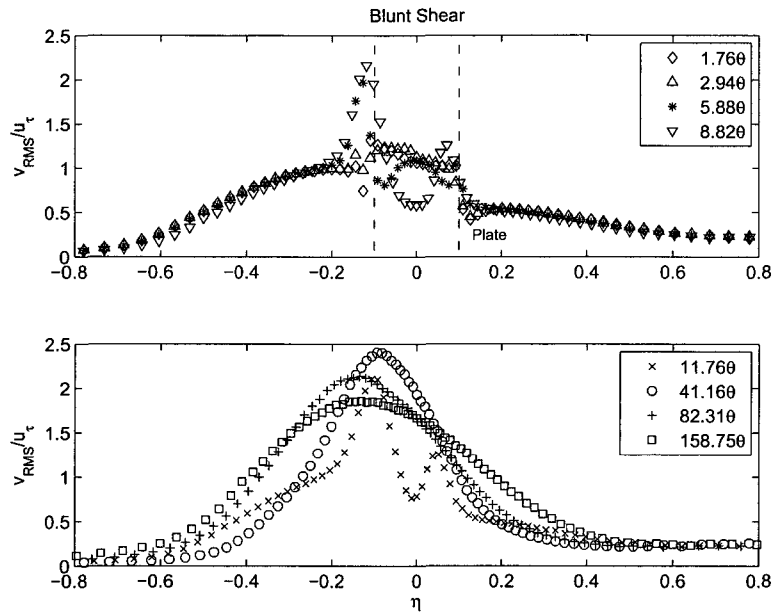

Figure 3-38: Fluctuating Wall Normal Velocity with increasing x/θ for BS case

The v_{RMS} profiles for the blunt edge with shear flow are shown in figure 3-38. The vertical dashed line in the first subplot denotes splitter plate edge. The profiles closest to the separation edge ($1.76 \leq x/\theta \leq 8.82$) have distinct peaks in the velocity fluctuations near the wall on the high speed stream side ($\eta = -0.12.$), and decrease in either direction. The peak on the slow speed side has moved towards the high speed side at a wall normal distance of $\eta = 0.07$. Further downstream, at $x/\theta = 11.76$, two separate peaks are still visible.

At a downstream distance of $x/\theta = 41.16$, the two peaks combine to form the largest magnitude of 2.41, at a wall normal location of $y/\delta_{sw} = -0.09$. Moving downstream from this point, a continuous decrease in peak magnitude but increase in width is observed with the peak located at a wall normal distance of $y/\delta_{sw} \simeq 0.13$.

3.4.3 Correlation Coefficients

The correlation coefficient, $\overline{uv}/u'v'$, is a useful measure of the level of flow organization The correlation coefficients for the sharp edge without shear, sharp edge with shear, and the blunt edge with shear cases are shown in figures 3-39, 3-40, and 3-41, respectively All of these are plotted versus the normalized wall normal coordinate η for increasing downstream distances (x/θ) The sharp edge without shear case shows very similar profiles for all downstream distances. A large region of constant correlation is observed between $-0.4 \leq x/\theta \leq 0.4$ with a sharp change in sign at $\eta = 0$. Outside of this region the correlation coefficients decrease almost to zero at $\eta = \pm 0\ 6$. After which, a slight but consistent increase in the freestream is seen.

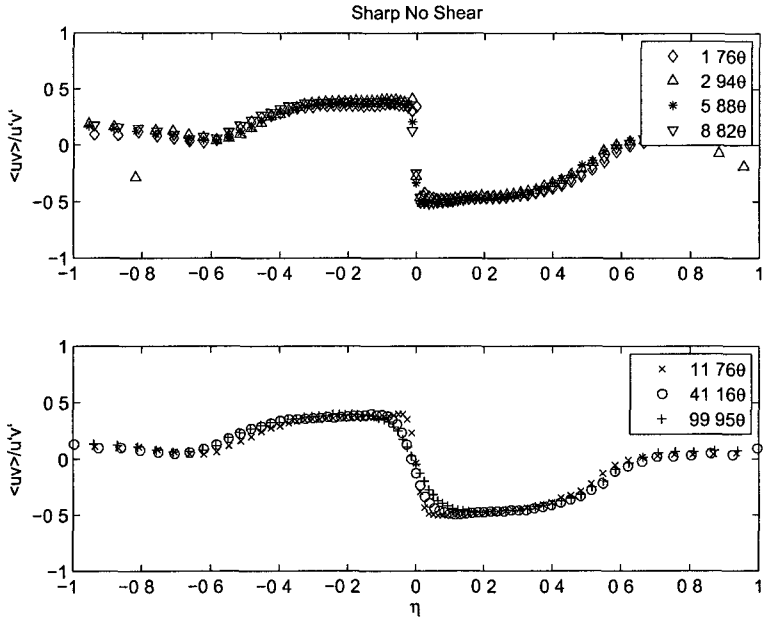

Figure 3-39· Correlation Coefficients with increasing x/θ for SNS case

The sharp edge with shear case contains the same constant correlation coefficient

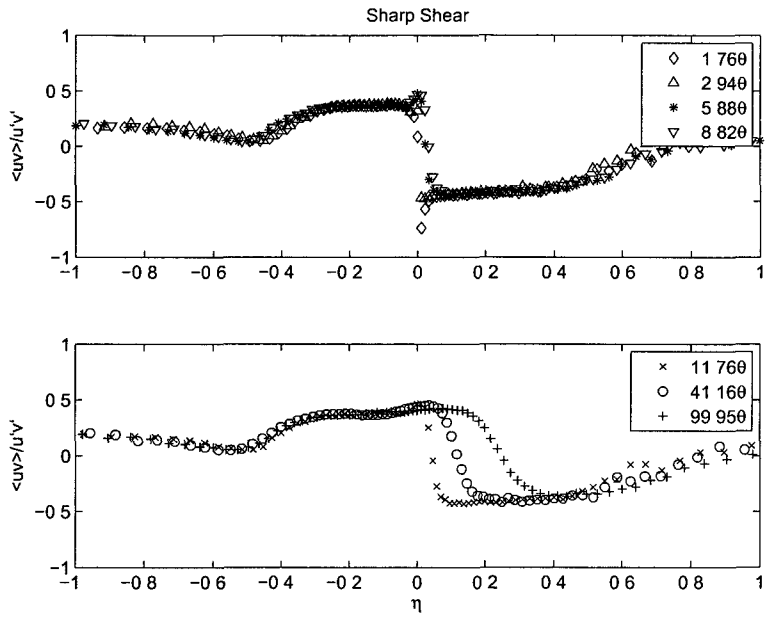

Figure 3-40: Correlation Coefficients with increasing x/θ for SS case

region as in the case without shear. A small peak occurs at $\eta = 0$ for downstream positions $x/\theta \leq 8.82$. Downstream, an extension of the constant correlation coefficients region towards the low speed side appears to occurs after $x/\theta = 11.76$. This extension continues to occur in the final downstream position of $x/\theta = 99.95$.

The correlation coefficients for the blunt edge with shear case are shown in figure 3-41 , where the vertical dashed lines denote the splitter plate walls. Near the separation edge ($x/\theta \leq 8.82$) there exists a smooth, slightly curved region on either side of the splitter plate wall with a peak right at the wall Directly behind the plate the profiles become scattered as previously observed. At $x/\theta = 11.76$, the near-wall peaks are easily observed, but have entirely vanished by $x/\theta = 41.16$. As seen in the previous two cases, the constant correlation coefficient region begin to extend towards the slow speed side at downstream distances greater than $x/\theta = 11.76$. This trend continues to the furthest downstream position of $x/\theta = 158.75$. This trend suggests that the slow speed flow is effectively

displaced by the high speed flow.

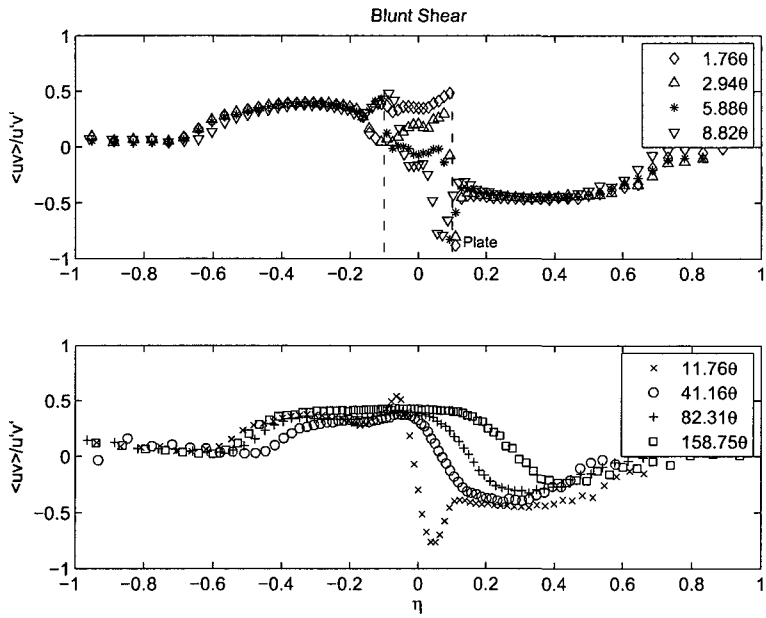

Figure 3-41: Correlation Coefficients with increasing x/θ for BS case

3.5 Mean Momentum Balance

The mean momentum balance was investigated for all three cases. Examination of the data revealed a region of rapid development just downstream of separation, followed by a much slower development for greater x/θ. In the following figures we examine data at $x/\theta = 1.76$ and $x/\theta = 5.88$. For greater downstream distances the ratio of the viscous stress gradient to the Reynolds stress gradient was, in all cases, found to be near zero for all wall normal distances. This indicates a balance between mean advection and the Reynolds stress gradient, except in a narrow zone about y_m^+. Since the plots examined are only in the "near-wall" region, the wall normal coordinate y^+ is employed (normalized by

u_τ from the high speed flow and μ). Measurements were taken in a logarithmic fashion to a wall normal distance of $y^+ \simeq 350$. Due to the absence of the wall downstream of the edge of separation, the origin of $y^+ = 0$ was set to the location on minimum velocity. As the momentum deficient region behind the plate fills in with downstream distance, this location of minimum velocity shifts according, thus making it appropriate for a new wall normal coordinate origin (see figure 3-13).

Prior to calculating the stress gradients, the U^+ and $< uv >^+$ profiles were smoothed using a Savitzky-Golay finite impulse response smoothing filter. The profiles were smoothed with a finite window size of five data points, and then derivatives were calculated using a central difference method. Note that only the zeroth-order profiles were smoothed using the S-G filter, not any of the subsequent gradients.

Each of the following figures are split up into three subplots: viscous stress gradient (B), Reynolds stress gradient (C), and the ratio of viscous stress gradient to Reynolds stress gradient (B/C). This presentation of each term allows for easier analysis of the four layers regime. The data can become relatively scattered away from the wall due to computing the ratio of two small values. Also, referencing the location where the Reynolds stress gradient first passes through zero gives rise to the location of the layer III discontinuity.

The mean momentum balances for the SNS case, are shown in figures 3-42 and 3-43. Closest to the separation edge ($x/\theta = 1.76$), it is observed that layer I, where the viscous stress gradient dominates, is nonexistent. The balance in layer II of viscous stress gradient to Reynolds stress gradient in a turbulent boundary layer is also not convincingly present. Instead, the Reynolds stress gradient is nearly ten times larger than the viscous stress gradient, creating a ratio near zero close to the wall ($y^+ < 25$). The peak in the Reynolds stress causes a discontinuity of layer III at $y^+ \simeq 25$. Further away from the wall ($y^+ > 25$), the ratio of terms becomes scattered about zero. This scattering of data

points is primarily due to taking the ratio of two profiles with magnitudes near zero.

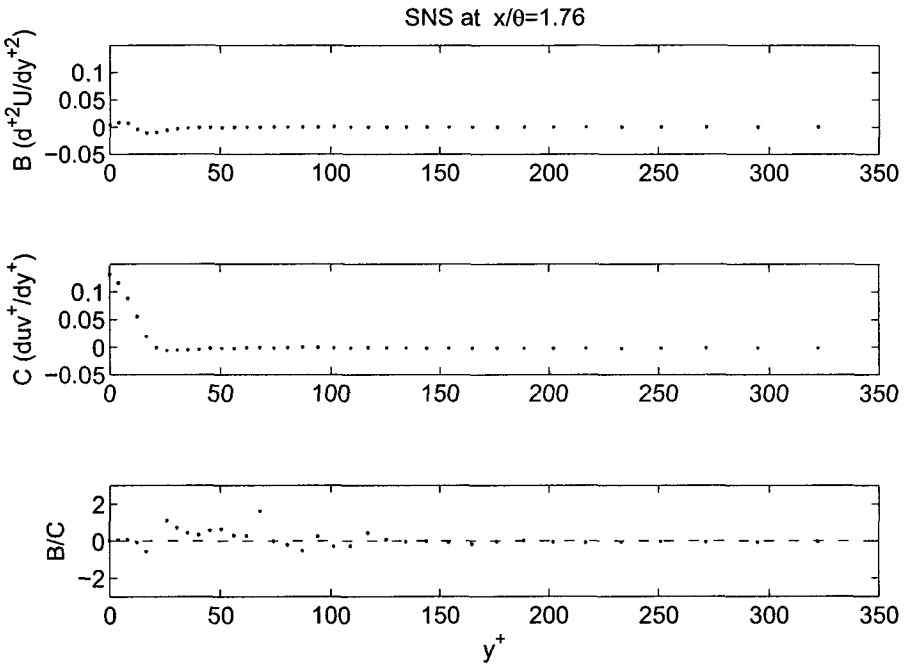

Figure 3-42: Mean Momentum Balance for SNS case at $x/\theta = 1.76$

At a downstream position of 5.88θ, the ratio of viscous stress gradient to Reynolds stress gradient for the SNS case is primarily zero for all y^+. At $y^+ \simeq 40$, a slight layer III discontinuity can still be seen due to the peak of the Reynolds stress. By this downstream distance, the Reynolds stress gradient and mean advection are in balance for essentially all y^+. Recall that this is the balance characteristic of free shear flow turbulence.

The mean momentum balances for the SS case, are shown in figures 3-44 and 3-45. At a downstream distance of 1.76θ, the ratio of terms near the wall ($y^+ < 25$) is almost zero. Unlike than the SNS case though, a slight increase right at the wall is observed. However, the Reynolds stress peak and discontinuity of layer III still occurs at $y^+ \simeq 25$ in both sharp edge cases. Outside of layer III ($y^+ > 25$), the ratio B/C trends to zero with

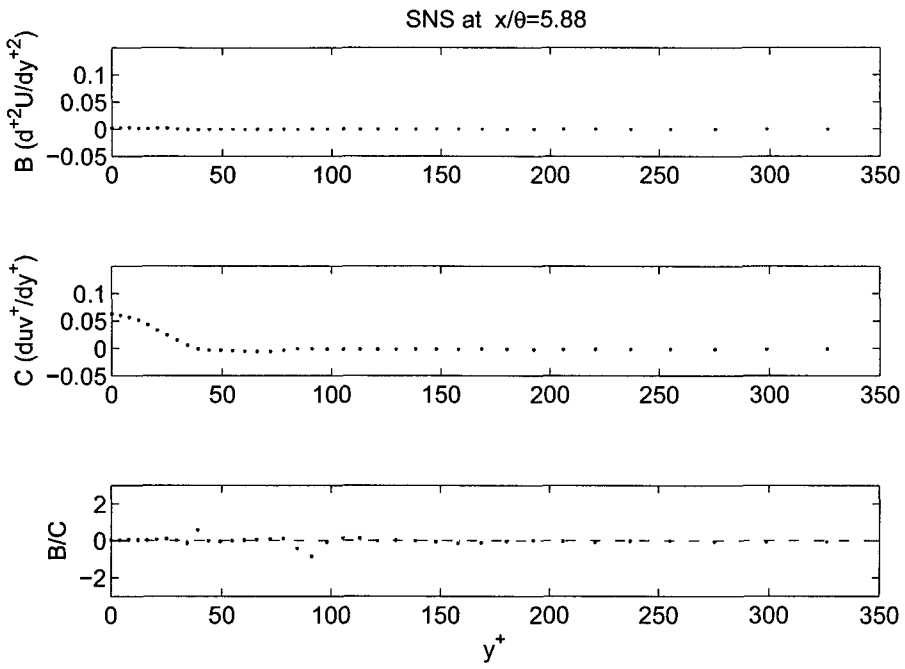

Figure 3-43: Mean Momentum Balance for SNS case at $x/\theta = 5.88$

some scattering due to the small magnitudes of B and C at this wall normal distance.

Further from the separation edge, at $x/\theta = 5.88$, the mean momentum balance is, once again primarily a balance between Reynolds stress gradient and mean advection for all y^+. The Reynolds stress gradient passes through zero at $y^+ \simeq 60$, creating a barely visible layer III discontinuity. Overall, it is easily observed that the viscous stress gradient is negligible, except in a small domain about y_m^+, by a downstream distance of 5.88θ.

The mean momentum balances for the BS case, are shown in figures 3-46 and 3-47. At a downstream distance of 1.76θ, the near-wall viscous sublayer present in the turbulent boundary layer is immediately obliterated in the shear wake flow. At $y^+ \simeq 21$ the Reynolds stress gradient passes through zero, which is where the discontinuity of layer III should be observed. However, the resolution of only 10 data points for $y^+ < 50$ makes it difficult to see. At $y^+ \simeq 47$, a large discontinuity occurs. Subsequently, estimates of

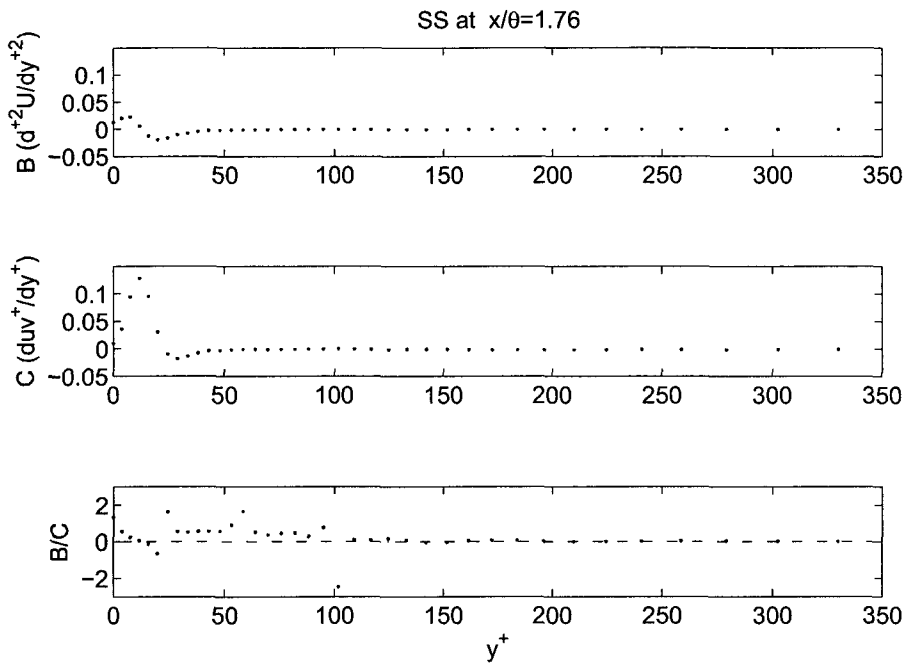

Figure 3-44: Mean Momentum Balance for SS case at $x/\theta = 1.76$

the peak Reynolds stress location found by Wei et al. (2005) scale with Reynolds number $y^+ \simeq 2 * \sqrt{\delta^+}$, which produces a value of $y^+ = 47.7$ [24]. However, this discontinuity is not the result of the first zero crossing in the Reynolds stress gradient. Away from the wall ($y^+ > 50$), the profile of B/C goes to zero, signifying a balance between mean advection and the Reynolds stress gradient.

At a downstream distance of 5.88θ, the Reynolds stress gradient dominates for all y^+. The remnant peak in the Reynolds stress causes the Reynolds stress gradient to pass through zero at $y^+ \simeq 45$. However, the viscous stress gradient has become too small to induce any visible layer III discontinuity. Though, if a finer resolution profile were acquired, it could reveal a slight discontinuity since the Reynolds stress gradient approaches zero at this point.

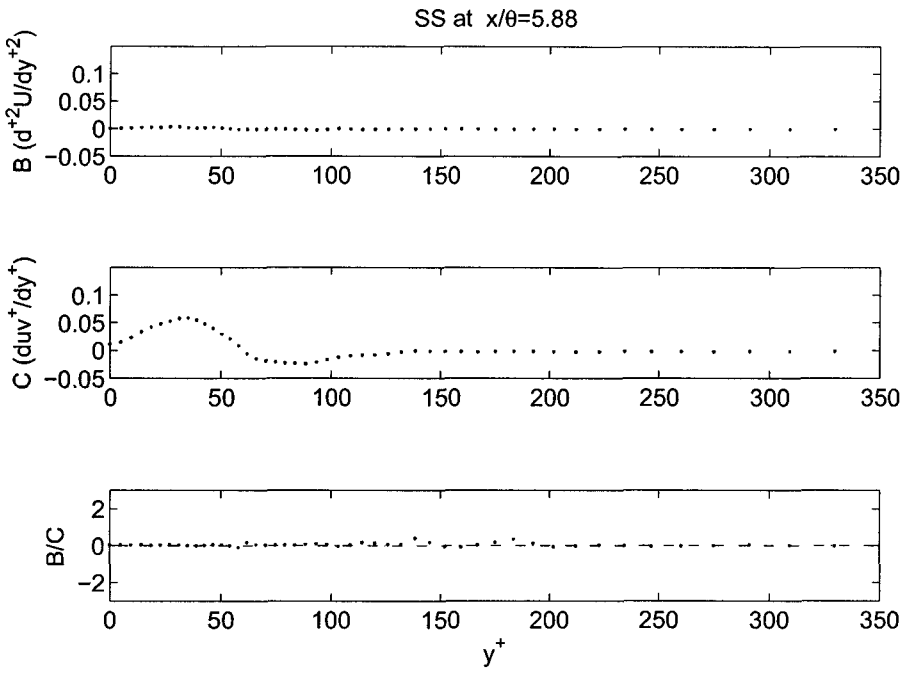

Figure 3-45: Mean Momentum Balance for SS case at $x/\theta = 5.88$

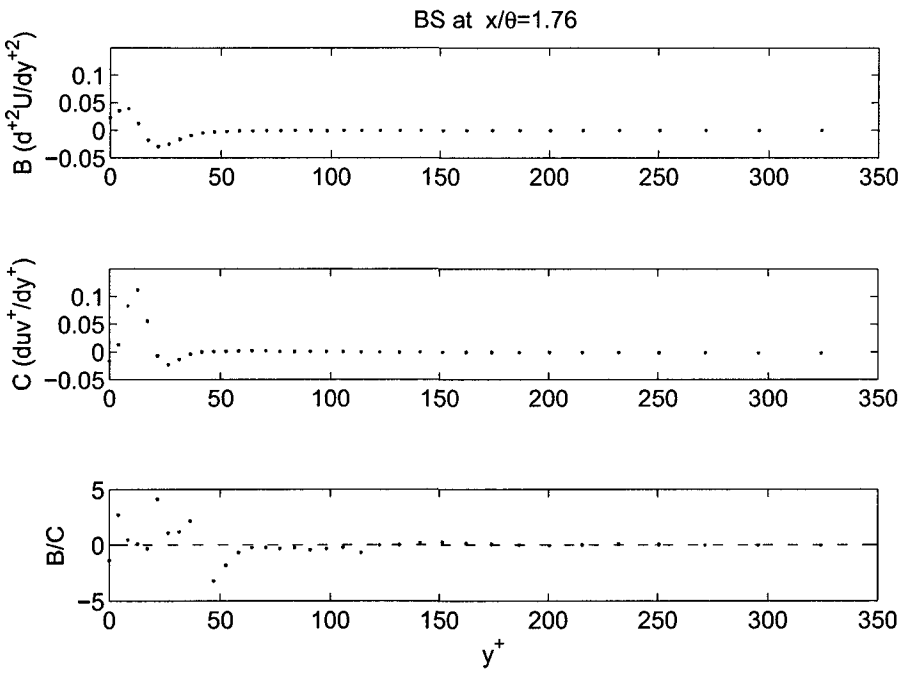

Figure 3-46: Mean Momentum Balance for BS case at $x/\theta = 1.76$

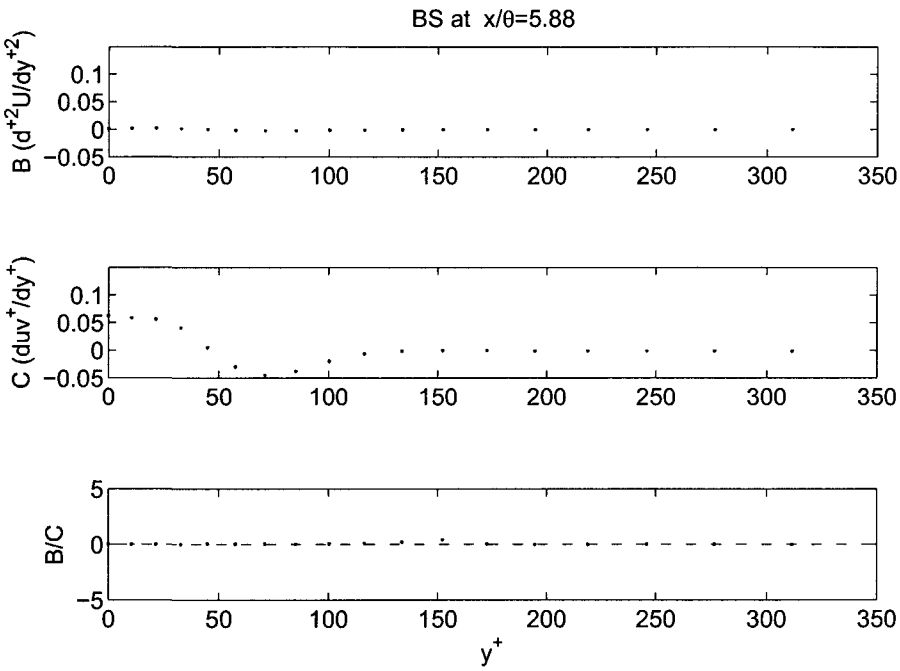

Figure 3-47: Mean Momentum Balance for BS case at $x/\theta = 5.88$

Chapter 4

Conclusions

This study intended to explore the evolution of the mean momentum balance in shear wake flows. Primary motivation was to explain the mean dynamics as the four-layer structure of the turbulent boundary layer observed in previous studies evolves into the mixing layer balance that is solely comprised of inertial terms. An experimental method was used by employing a two layer shear tunnel that contained two converging turbulent boundary layer flows with varying trailing edge geometries and flow velocities. The data was acquired by traversing a using a four-element hotwire probe at a number of downstream locations from the separation edge. From these experiments the primary conclusions are derived.

1. Although the profile data comparisons at $x/\theta = 1.76$ to DNS turbulent boundary layer data were reasonable, it is apparent that the turbulent boundary layers of the present study were significantly distorted by $x/\theta = 1.76$. For the sharp edge geometries, it is also likely that the profiles were distorted prior to separation owing to the adverse pressure gradient caused by the diverging wall. At the measurement location of $x/\theta = 1.76$, the blunt edge case replicated the canonical boundary layer flow properties more precisely than in the sharp edge flows. These results have similarity to those by Morris and Foss (2003) [17].

2. The present data provide evidence that the location of the peak in the Reynolds stress, y_m^+, approximately scales like $y_m^+ \simeq \sqrt{\delta^+}$ for shear-wake flow. This location

is proportional to but approximately half that found in turbulent boundary layer studies.

3. For $x/\theta > 10$, the rate at which the wake component diminishes with downstream distance was found to well approximated by a power law fit (see figure 3-12). In both shear cases, the slope was interpolated to indicate a free shear flow emerged near $x/\theta = 200$. The diminishing distance drastically increased to approximately 1400θ in the absence of shear.

4. The Reynolds stress peaks in the pure wake case reached a value near unity, which is comparable with the turbulent boundary layer maximum. Close to separation ($x/\theta = 1.76$), the y_m^+ value (peak distance from wall in y^+ units) is about 23. Turbulent boundary layer data at similar Reynolds number ($\delta^+ = 660$) produced a similar $y_m^+ \simeq 26$ [11]. The peak Reynolds stress position versus downstream distance for the pure wake case was found to scale with a power law (slope of 0.87). In the cases with shear there is a secondary peak that attains values significantly greater in magnitude than in the turbulent boundary layer alone. This peak location remains at an essentially fixed y-location, close to the wall, for all measured downstream distances.

5. The Reynolds stress correlation coefficient measurements indicated peak values close to those found in the boundary layer for all flows investigated. Examination of the velocity intensities reveal that the v'^+ approximately scales with $< uv >^+$.

6. In all three cases, the mean momentum balance data reveal that layers I and II are obliterated by the closest downstream measurement location ($x/\theta = 1.76$). This is primarily due to the peak in the Reynolds stress gradient being about ten times larger in magnitude than the viscous stress gradient. However, a remnant peak in the Reynolds stress is retained for downstream locations $x/\theta \lesssim 8$.

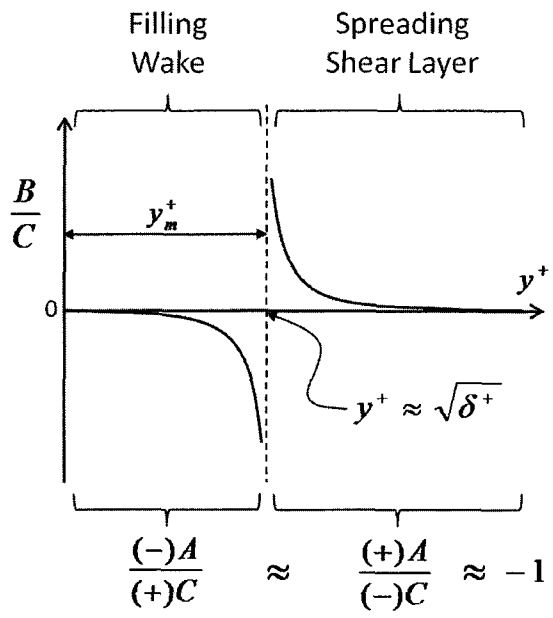

Figure 4-1: Mean momentum balance of shear wake close to the separation edge ($x/\theta = 1.76$)

7. Considering that there are only three terms in the mean momentum balance (1.7), the ratio of stress gradients (B/C) being mostly zero indicates in the shear wake flow that there must be a balance between mean advection (A) and the Reynolds stress gradient (C) everywhere, except in a narrow zone about y_m^+. The depiction of figure 4-1 illustrates that the ratio of mean advection (A) to Reynolds stress gradient (C) must be equal to approximately negative unity everywhere, except near y_m^+. (Note that for simplicity this analysis considers the region y ¿ 0.) Interior to y_m^+, the Reynolds stress gradient is positive and thus the mean advection term must be negative. This indicates that the net momentum transport is inward towards $y = 0$ (filling in the wake deficit). Exterior to y_m^+, the Reynolds stress gradient is negative and thus the mean advection term is positive. Thus the net momentum transport is outward for $y > y_m$ (spreading the shear layer).

Bibliography

[1] H.H. Bruun. *Hot-wire Anemometry,*. Oxford Science Pubs, 1996.

[2] D. Challa. On the downstream evolution of turbulent intial condition shear-wake flows. Master's thesis, University of Utah, August 2005

[3] R. Clark. Evaluation of subgrid-scale models using an accurately simulated turbulent flow. *Journal of Fluid Mechanics*, 91:1–16, 1979.

[4] F. Clauser. Turbulent boundary layers in adverse pressure gradients. *Journal of Aeronautical Sciences*, 21(2):91–108, 1954.

[5] W. J. Dahm, C. E. Frieler, and G. Tryggvason. Vortex structure and dynamics in the near field of a coaxial jet. *Journal of Fluid Mechanics*, 241:371–402, 1992.

[6] P.A. Davison, editor. *Turbulence.* Oxford, New York, 2004.

[7] J. Hamelin E. and Alving Amy. A low-shear turbulent boundary layer. *Phys. Fluids*, 8:789–804, 1995.

[8] Robert Fox, Alan McDonald, and Philip Pritchard. *Introduction to Fluid Mechanics.* Wiley, 6 edition, 2004.

[9] R. W. Johnson. *Handbook of Fluid Dynamics.* CRC Press Web, 1998.

[10] F.E. Jorgensen. Directional sensitivity of wire and fiber-film probes *DISA Inform*, 11, 1971.

[11] J. Klewicki, R. Ebner, and X. Wu. Mean dynamics of transitional boundary layer flow. *Journal of Fluid Mechanics*, 2011.

[12] Joe Klewicki, Paul Fife, Tie Wei, and Pat McMurtry. A physical model of the turbulent boundary layer consonant with mean momentum balance structure. *Philosophical Transactions of the Royal Society A: Mathematical, Physical and Engineering Sciences*, 365(1852):823–840, 2007.

[13] A. Kwan and N. Ko. The initial region of subsonic coaxial jet. *Journal of Fluid Mechanics*, 73:305–332, 1976.

[14] A. Kwan and N. Ko. The initial region of subsonic coaxial jets. part 2. *Journal of Fluid Mechanics*, 82:273–287, 1977.

[15] F. Mehdi, J. Klewicki, and C. White. Mean momentum balance analysis of rough-wall turbulent boundary layer. *Physica D: Nonlinear Phenomena*, 239:1329–1337, 2009.

[16] R. Mehta. Effect of velocity ratio on plane mixing layer development· Influence of the splitter plate wake. *Experiments in Fluids*, 10:194–204, 1991.

[17] S. Morris and J. Foss. Turbulent boundary layer to single-stream shear layer: The transition region. *Journal of Fluid Mechanics*, 494:187–221, 2003.

[18] S. Pope. *Turbulent Flows.* Cambridge University Press, Cambridge, UK, New York, 2000.

[19] Schlatter and Orlu. Dns of a turbulent zero-pressure gradient. *Bulletin APS*, 54:19:59, 2009.

[20] K. R. Sreenivasan. The turbulent boundary layer. In M. Gad-el-Hak, editor, *Frontiers in Experimental Fluid Mechanics*, pages 159–209, 1989.

[21] C. Tropea, A. Yarin, and J. Foss. *Handbook of Experimental Fluid Mechanics.* Springer, Berlin, 2007.

[22] P. Vukoslavcevic, J. Wallace, and J.L. Balint. The velocity and vorticity vector fields of a turbulent boundary later. part 1. simultaneous measurements by hot-wire anemometry. *Journal of Fluid Mechanics*, 228:25–51, 1991.

[23] J. Wait. On the downstream evolution of laminar intial condition shear-wake flows. Master's thesis, University of Utah, December 2003.

[24] T. Wei, P. Fife J. Klewicki, and P. McMurtry. Properties of the mean momentum balance in turbulent boundary layer,pipe and channel flows. *Journal of Fluid Mechanics*, 552:303–327, 2004.